

KEK Preprint 2017-25

August 2017

A

Construction and commissioning of the compact energy-recovery linac at KEK

Submitted to Nuclear Instruments and Methods in Physics Research Section A



High Energy Accelerator Research Organization

High Energy Accelerator Research Organization (KEK), 2017

KEK Reports are available from:

High Energy Accelerator Research Organization (KEK)
1-1 Oho, Tsukuba-shi
Ibaraki-ken, 305-0801
JAPAN

Phone: +81-29-864-5137

Fax: +81-29-864-4604

E-mail: irdpub@mail.kek.jp

Internet: <http://www.kek.jp>

Construction and commissioning of the compact energy-recovery linac at KEK

Mitsuo Akemoto^{a,b}, Dai Arakawa^a, Seiji Asaoka^a, Enrico Cenni^{b,1}, Masato Egi^a, Kazuhiro Enami^a, Kuninori Endo^a, Shigeki Fukuda^a, Takaaki Furuya^a, Kaiichi Haga^{a,b}, Ryoichi Hajima^{c,d}, Kazufumi Hara^a, Kentaro Harada^{a,b}, Tohru Honda^{a,b}, Yosuke Honda^{a,b}, Teruya Honma^a, Kenji Hosoyama^a, Eiji Kako^{a,b}, Hiroaki Katagiri^a, Hiroshi Kawata^{a,b}, Yukinori Kobayashi^{a,b}, Yuuji Kojima^a, Yoshinari Kondou^a, Olga Tanaka^a, Tatsuya Kume^{a,b}, Masao Kuriki^e, Hiroshi Matsumura^{a,b}, Hideki Matsushita^a, Shinichiro Michizono^{a,b}, Takako Miura^{a,b}, Tsukasa Miyajima^{a,b}, Shinya Nagahashi^a, Ryoji Nagai^{c,d}, Hirotaka Nakai^{a,b}, Hiromitsu Nakajima^a, Norio Nakamura^{a,b}, Kota Nakanishi^{a,b}, Kazuyuki Nigorikawa^a, Nobuyuki Nishimori^f, Takashi Nogami^a, Shuichi Noguchi^a, Takashi Obina^{a,b}, Feng Qiu^{a,b}, Hidenori Sagehashi^a, Hiroshi Sakai^{a,b}, Shogo Sakanaka^{a,b,*}, Shinichi Sasaki^{a,b}, Kotaro Satoh^a, Masaru Sawamura^{c,d}, Miho Shimada^{a,b}, Kenji Shinoe^{a,2}, Toshio Shishido^a, Mikito Tadano^a, Takeshi Takahashi^a, Ryota Takai^{a,b}, Tateru Takenaka^a, Yasunori Tanimoto^{a,b}, Takashi Uchiyama^a, Akira Ueda^a, Kensei Umemori^{a,b}, Ken Watanabe^{a,b}, Masahiro Yamamoto^{a,b}

^a KEK, High Energy Accelerator Research Organization, 1-1 Oho, Tsukuba, Ibaraki 305-8001, Japan

^b SOKENDAI, The Graduate University for Advanced Studies, Hayama, Kanagawa 240-0193, Japan

^c JAEA, Japan Atomic Energy Agency, Tokai, Naka, Ibaraki 319-1195, Japan

^d QST, National Institutes for Quantum and Radiological Science and Technology, Tokai, Naka, Ibaraki 319-1106, Japan

^e Hiroshima University, Higashihiroshima, Hiroshima 739-8530, Japan

^f Tohoku University, Aoba-ku, Sendai 980-8577, Japan

¹ Present address: CEA, Irfu, SACM, Centre de Saclay, F-91191 Gif-sur-Yvette Cedex, France

² Deceased, September 2015.

* Corresponding author. E-mail address: shogo.sakanaka@kek.jp

Phone: +81-29-864-5668, FAX: +81-29-864-2801

Abstract

Energy-recovery linacs (ERLs) are promising for advanced synchrotron light sources, high-power free electron lasers (FELs), high-brightness gamma-ray sources, and electron-ion colliders. To demonstrate the critical technology of ERL-based light sources, we have designed and constructed a test accelerator, the compact ERL (cERL). Using advanced technology that includes a photocathode direct current (DC) electron gun and two types of 1.3-GHz-frequency superconducting cavities, the cERL was designed to be capable of recirculating low emittance (≤ 1 mm·mrad) and high average-current (≥ 10 mA) electron beams while recovering the beam energy. During initial commissioning, the cERL demonstrated successful recirculation of high-quality beams with normalized transverse emittance of ~ 0.14 mm·mrad and momentum spread of $\sim 1.2 \times 10^{-4}$ (rms) at a beam energy of 20 MeV and bunch charge below 100 fC. Energy recovery in the superconducting main linac was also demonstrated for high-average-current continuous-wave beams. These results constitute an important milestone toward realizing ERL-based light sources.

Keywords: Energy recovery linac, ERL, ERL x-ray source, Photocathode DC gun, Superconducting cavity, High brightness beam

1. Introduction

In advanced energy-recovery linacs (ERLs), high-brightness electron beams are produced using a photo-injector and are accelerated by superconducting (SC) cavities. Beams are then used to produce synchrotron radiation (SR) or for other applications. Spent beams are decelerated while recovering their energy, and are dumped at low energy. Since the rf-power requirement for beam acceleration is significantly spared and the risk of radiation hazard at the dump is significantly reduced, ERLs are very suitable for boosting the beam intensity of high-brightness electron linacs by several orders of magnitude.

The concept of ERL was first suggested by Tigner [1] and implemented in high-power free electron lasers (FELs) [2–4]. Because the beams in ERLs are less affected by successive emission of incoherent or coherent SR along a recirculation loop, electron beams can reach extremely low emittances that are close to the diffraction limit for hard x-rays. It is also possible to compress the electron bunches down to a hundred femtoseconds at high repetition rates. These features are very advantageous for future light sources that are expected to provide high-brightness SR and/or ultra-short x-ray pulses [5], as well as for advanced high-power FELs. The ERLs are also expected in nuclear and high-energy physics for applications in electron-ion colliders [6, 7], electron cooling of hadron beams [6], and high-brightness gamma-ray sources [8].

Multi-GeV ERL-based x-ray sources have been proposed by several institutes [9–13]. One of the plans [12, 13], which we proposed at the High Energy Accelerator Research Organization (KEK), is to construct a 3-GeV ERL for use as a super-brilliant synchrotron light source, as well as for extending it to a driver for a proposed x-ray free-electron-laser oscillator (X-FELO) [14]. This project requires normalized beam emittances of 0.1–1 mm·mrad with the average beam current in the 10–100 mA range. In addition, beams should be sufficiently stable in both position and intensity, and the beam-loss ratio in the recirculation loop should be extremely small, at most 10^{-7} . Such projects are associated with considerable challenges in accelerator physics and technology, which are typically summarized in [15].

Some major technological challenges associated with ERL-based x-ray sources are: (1) high-brightness photo-emission electron guns capable of producing ultra-low emittance beams with high average currents that would persist for a long period of time; (2) a laser system for illuminating the photocathode with an average power of ~ 100 W,

with sufficient spatial and temporal stability; (3) SC cavity for an injector, for providing high rf power to beams with moderate accelerating gradients; and (4) another SC cavity for the main linac (ML), with high unloaded-Q at an accelerating gradient of 15–20 MV/m, while damping higher-order modes for avoiding beam breakup (BBU) instabilities. The challenges associated with accelerator physics are: (5) transportation of high-brightness beams with minimal degradation of emittance under the space-charge force, rf fields, coherent synchrotron radiation (CSR), and trapped ions; (6) understanding the formation of beam halos and their effective collimation; (7) diagnostics of beams with high average currents; and (8) stabilization of beams, especially at the source. Powerful simulation techniques based on accurate accelerator modeling are essential for predicting these issues, but these simulations should be validated using real machines. Therefore, there is a strong need to construct an ERL test facility where these critical technologies can be demonstrated, as well as to study accelerator physics issues relevant to ERLs.

For the above-mentioned purposes, several ERL test facilities have been constructed [16–19], are under construction [20], or being designed [21]. Among these, the team working on the Cornell ERL injector prototype [16] has successfully generated 8-MeV-energy beams with the 90% normalized emittances of approximately 0.29–0.51 mm·mrad for a bunch charge of 77 pC, and obtained the maximum average beam current of 65 mA. On the other hand, our Japanese collaboration team (that includes KEK, JAEA and other institutes) has developed [22] critical components, including a photocathode direct current (DC) electron gun and two types of SC cavities in an R&D effort that started in 2006. Then, we constructed a test accelerator, the compact ERL (cERL) [23], at KEK. The cERL contains most of the critical components for the ERL-driven x-ray source, including the recirculation loop, and it allows us to test all of these components together as well as to study accelerator physics issues specific to ERLs. In this paper, we present the design, construction, and initial commissioning results of the cERL. We describe the basic design and subsystems of cERL in Secs. 2 and 3, respectively, and briefly report on the progress of construction in Sec. 4. We present the results of initial commissioning in Sec. 5, and discuss the present performance in Sec. 6.

2. Design of the compact ERL

2.1 Concept

The compact ERL aims to establish the critical technology needed for constructing the ERL-based x-ray source. A primarily important issue is the production and transportation of high-brightness electron beams. The cERL is illustrated in Fig. 1. The cERL consists of an injector and a recirculation loop that includes the ML. An electron beam is generated at a photocathode DC gun and is pre-accelerated up to the energy of ~ 5 MeV using three 2-cell SC cavities in an injector cryomodule. The beam is merged into a recirculation loop and further accelerated up to 35 MeV using two 9-cell SC cavities in the ML cryomodule. The beam is transported through the recirculation loop, decelerated in the ML for energy recovery, and separated into a dump line. The beam from the injector can also be transported into an injector-diagnostic line where various beam parameters can be measured.

*** Fig. 1 ***

Since the cERL includes all of the fundamental components of the ERL, it allows us to operate them all together in an actual accelerator environment while conducting accelerator-physics studies needed to establish the ERL technology. The cERL is also valuable for developing beam tuning methods and diagnostic techniques using real ERL beams.

Our goals for the cERL are listed in Table 1. Considering both the radiation issues in an available building and the present power-handling capability of injector couplers, the beam current of 10 mA was chosen as a present goal. Some of the components, including the ML cryomodule, were designed considering a future upgrade of the beam current to 100 mA. The beam energy goal is 35 MeV, which is available with a single ML cryomodule. The beam energy can be upgraded if additional ML cryomodules are installed in available space in the north-straight section (Fig. 7). Target normalized emittance of 0.3 (1) mm-mrad at a bunch charge of 7.7 (77) pC corresponds to the beam emittance of 50 (170) pm-rad at an average beam current of 10 (100) mA in the future 3-GeV ERL x-ray source, where the parameters in parentheses denote those for the high-flux operation mode. In the 3-GeV ERL, we aim at further reducing the beam emittance, e.g., by increasing the injection energy.

*** Table 1 ***

2.2 Injector

In the injector, high-brightness and high-average-current beams should be generated, pre-accelerated, and transported to the ML, while preserving high beam quality. As a high-brightness electron source, we employed a gallium arsenide (GaAs) photocathode with a negative electron affinity (NEA) surface. The normalized rms emittance of the beam that was generated by the photocathode is given by [24]

$$\varepsilon_{nx} = \sigma_{x,L} \sqrt{\frac{2\langle E_{kx} \rangle}{mc^2}}, \quad (1)$$

where $\sigma_{x,L}$ is the rms laser spot size on the cathode, $\langle E_{kx} \rangle$ is the initial mean transverse energy (MTE) of the generated beam, and m and c are the electron's mass and the speed of light, respectively. The MTE depends on the cathode material and the wavelength of cathode-excitation laser. The MTE of GaAs for the laser's wavelength of 544 nm was measured to be 60 meV [24]. With a spot size of $\sigma_{x,L} = 0.275$ mm, for example, an initial normalized emittance of 0.13 mm·mrad is expected. Therefore, the GaAs photocathode could generate high-brightness beams, meeting the target performance goal of the cERL.

Figure 2 schematically shows the cERL injector. An electron beam, generated by the photocathode, is accelerated to the kinetic energy of 500 keV by the DC gun. The beam is transported through a low-energy beam transport where two solenoid magnets and a buncher cavity are located. The solenoids are used to adjust the beam optics while the buncher cavity is used to compress the bunch length. The beam is then accelerated through the injector cavities up to a total energy of ~5.5 MeV, and is transported to the ML through a merger section. Five quadrupole magnets are used to adjust the beam optics between the injector cavities and the merger section.

*** Fig. 2 ***

Because of the low beam energy in the injector, the beam motion is largely influenced by self-forces due to the space charge effect, which increases both the emittance and the bunch length. The time-dependent focusing force due to the rf field affects the beam as well. The beam dynamics in the injector is complicated because the transverse and longitudinal motions are correlated due to these effects. Thus, it is important to control the beam dynamics in the six-dimensional phase space. To find the optimal design parameters of the injector, we used a combination of particle tracking simulations and an optimization method. The goal of the injector optimization process

was to simultaneously minimize the emittance and the bunch length while satisfying the optics-matching condition required for the recirculation loop.

For optimization, we used a genetic algorithm-based multi-objective method [25]. This method is advantageous because it allows us to simultaneously optimize multiple objects (in our case, the normalized emittance and the bunch length). For particle tracking simulations, we used the General Particle Tracer (GPT) [26] with a mesh-based space charge routine and an enhanced space charge routine [27] for improving the simulation accuracy in the merger section. The simulations were conducted in parallel, and optimization was performed over 50 populations generated by the genetic algorithm. The optimization was conducted in two stages. First, we optimized the position of each component of the injector assuming a bunch charge of 80 pC, which is slightly higher than the maximum bunch charge of 77 pC in Table 1. Next, we optimized the injector optics assuming a bunch charge of 7.7 pC, which is used during early stages of commissioning.

In the first stage, we assumed a bunch charge of 80 pC and minimized the emittance and the bunch length at the exit from the merger while varying the parameters including the positions of components listed in Table 2. After this optimization, the horizontal and vertical emittances were obtained as functions of the bunch length, and are shown in Fig. 3. Based on this result, we fixed the positions of the components, as shown in Table 2 and Fig. 4.

*** Fig. 3 ***

*** Fig. 4 ***

*** Table 2 ***

In the second stage, we optimized the injector optics for the bunch charge of 7.7 pC. To speed up the convergence, we conducted the optimization in three steps, which correspond to the following three sections: 1) the injector section, 2) the merger section, and 3) the ML section.

In the first step of the second stage, we tentatively optimized the parameters of the injector section so that the emittance and the bunch length at the exit from the injector section were minimized. The free parameters that we used were: the initial pulse length and the spot size of the laser, the strengths of the two solenoid magnets, the amplitudes and phases of the buncher cavity and injector cavities, respectively. The result of this optimization is shown in Fig. 5. For the bunch length of 0.59 mm, the horizontal and

vertical normalized emittances were 0.161 and 0.167 mm·mrad, respectively.

*** Fig. 5 ***

In the second step, we optimized both the parameters of the injector section and the strengths of five quadrupole magnets before the merger, for minimizing the emittance at the exit from the merger. The injector parameters, which were optimum at the bunch length of 0.59 mm (1.97 ps), were taken as initial parameters. As a result, we obtained the normalized emittance of 0.23 mm·mrad in both horizontal and vertical directions at the exit from the merger section.

In the third step, we optimized all parameters up to the ML section. We required that the Twiss parameters at the exit (hereafter, point A) from the ML section should range within: $-0.3 < \alpha_x < -0.1$, $2.5 < \alpha_y < 3.5$, $1 \text{ m} < \beta_x < 5 \text{ m}$, and $2 \text{ m} < \beta_y < 18 \text{ m}$, which is required from the optics design of the recirculation loop. The result of the optimization is shown in Fig. 6. The horizontal and vertical normalized emittances at the point A were 0.26 and 0.27 mm·mrad, respectively. The optimized parameters are listed in Table 3.

*** Fig. 6 ***

*** Table 3 ***

Sometimes there is a need to change some accelerator parameters, such as the bunch charge, the gun voltage, or the beam energy of the injector. During the first commissioning of the cERL, for example, we adopted the gun voltage of 390 kV instead of 500 kV, and the injector beam energy was 2.9 MeV instead of 5.5 MeV, as is mentioned in Sec. 4. We can adapt the parameters to such modifications by conducting the above-mentioned three-step optimization again.

2.3 Recirculation loop

The cERL beamline is schematized in Fig. 7. The beam merges into the recirculation loop that comprises two arc sections and both north- and south-straight sections. The north-straight section functions to: (1) match the injected beam to the ML, (2) accelerate and decelerate the beam in the ML on the first and the second passages, respectively, (3) match the decelerated beam to the dump line for minimizing the beam size in the dump line, and (4) match the beam optics in the north-straight section to those in the two arcs. The south-straight section functions to: (5) transport the beam from the first to the second arc, (6) change the path length using a chicane, (7) focus the beam sizes at an

interaction point when the laser Compton scattering (LCS) experiment [28] is conducted, and (8) match the optics to the LCS section.

*** Fig. 7 ***

As described in Sec. 2.2, the design of the beamline ranging from the electron gun to the exit point (point A in Fig. 7) of the ML was optimized for minimizing the emittance growth due to the space-charge effect. The beamline past point A was designed using the computer code *elegant* [29], without the space charge effect. The beam optics of the recirculation loop was designed to preserve small beam emittance along the beamline, as well as to ensure moderately small beam sizes. The magnets that were used in the lattice are described in Sec. 3.6.

The merger consists of three dipole magnets. The last of them, which is common with both injected and recirculated beams, deflects the injected beam by 16° , while it deflects the recirculated beam by $(p_i/p_r) \cdot 16^\circ$, where p_i and p_r are the momenta of the injected and recirculated beams, respectively. The kick to the recirculated beam is compensated by arranging two other dipoles in the recirculation loop, by which an injection chicane is formed. A similar scheme (dump chicane) is also used for extracting the beams. Due to a finite aperture at the injection chicane, the momentum ratio (p_i/p_r) is limited to be 1/6 or less. Under nominal design, the total energies of the injected and recirculated beams are 5.5 MeV and 35 MeV, respectively.

Each arc section consists of four 45° bending magnets and six quadrupoles, as shown in Fig. 8. Each arc is essentially the triple-bend achromat (TBA) lattice if the central two bends are considered as a single bend. The TBA lattice is to be used for the 3-GeV ERL [12], and choosing a similar lattice is advantageous for our experience. Similar to the conventional TBA lattice, we assumed a mirror-symmetric optics about the center of the arc, by which the strengths of the quadrupoles Q4 to Q6 were determined according to those of the quadrupoles Q3 to Q1. In designing the arc optics, we imposed both achromat and isochronous conditions, with the latter required for maintaining the longitudinal bunch profile. Then, there is only one degree of freedom in the quadrupole strengths. If we select one of the elements, R_{11} , of the 6-dimensional transfer matrix through the arc as a free parameter, we can determine the set of K -values of all of the quadrupoles as a function of R_{11} . The result is shown in Fig. 9. Both DFD (defocus-focus-defocus) and FDF (focus-defocus-focus) configurations are possible for each triplet of the quadrupoles. We found that the R_{11} values in the 0.6–1.4 range are

suitable because they result in an adequately small vertical betatron function (β_y) at both ends of the arc.

*** Fig. 8 ***

*** Fig. 9 ***

Once a set of quadrupoles (Q1 to Q6) has been tentatively selected, we have four degrees of freedom associated with the initial Twiss parameters ($\alpha_x, \beta_x, \alpha_y, \beta_y$). We assumed that the horizontal and vertical betatron functions are symmetric about the center of the arc, that is, $\alpha_x = \alpha_y = 0$ at the center. For the remaining two parameters, we considered the horizontal and vertical betatron functions ($\beta_{x,c}$ and $\beta_{y,c}$) at the center of the arc. Then, we optimized the parameter $\beta_{x,c}$ based on tracking simulations that included CSR wakes. Figure 10 shows the result of these tracking simulations from the entrance to the exit of the arc. In this figure, the normalized horizontal emittance at the exit from the arc is shown as a function of $\beta_{x,c}$, where R_{11} was set to 0.687. The assumed parameters were: the beam energy was 35 MeV; the initial distribution of particles was Gaussian, with the normalized emittance of 0.4 mm-mrad; the initial rms bunch length was 3 ps; the bunch charge was 80 pC. We set $\beta_{x,c} = 5$ m where the emittance growth due to CSR wakes could be minimized. We also found that setting R_{11} to be in the 0.1–1.4 range did not change the result in Fig. 10. By trial and error, we set $R_{11} = 0.687$, which fit the overall optics design of the recirculation loop.

*** Fig. 10 ***

It is worth noting that an application of optimization techniques based on linearized theory, presented in [30–32] for example, is not straightforward in the case of the cERL. This is because the CSR wake potential changes its shape along with the variation in the longitudinal bunch profile through the TBA cell, due to its small bending radius (1 m), large bending angle ($45^\circ/\text{dipole}$), and low beam energy (35 MeV).

The other free parameter, $\beta_{y,c}$, can be determined somewhat arbitrarily. We chose $\beta_{y,c} = 5$ m because this resulted in reasonably small β_y at both ends of the arc section. Thus, the designed optics of the arc is shown in Fig. 11.

*** Fig. 11 ***

When we compress the bunch length, each bunch is accelerated at an off-crest phase in the ML. The bunch is then compressed along the first arc under non-isochronous beam optics. For this purpose, we need to change the matrix element, R_{56} , through the arc, which is given by

$$R_{56} = \int_{Arc} \frac{\eta_x(s)}{\rho(s)} ds, \quad (2)$$

where η_x and ρ are the horizontal dispersion function and the curvature radius, respectively. In this case, we can take the dispersion function, $\eta_{x,c}$, at the center of the arc, as a free parameter instead of the isochronous condition. Then, we can change R_{56} appropriately as a function of $\eta_{x,c}$.

To fully recover the beam energy, the path length of the recirculation loop should be adjusted accurately so that every bunch passes the ML 180° out of phase on the second passage. We designed the path length of the loop so that the recirculated beam is decelerated at a correct phase while considering the precise speed of the particles. In addition, we arranged two mechanisms for adjusting the path length. One is an orbit bump in each arc section. As illustrated in Fig. 12, an orbit bump is produced using four horizontal kicks that are produced using two sub-coils of the main bending magnets and two path-length-control steering magnets. The latter magnets were initially substituted by sub-coils of the quadrupole magnets. Using this method, the path length can be changed by ± 10 mm per each arc. An application of this method is described in Sec. 5.1. The other mechanism is a path-length-control chicane, consisting of four dipoles in the south-straight section, by which the path length is changed within ± 5 mm. We found later that the latter method is less easy to handle due to some problems such as large hysteresis of the chicane magnets.

*** Fig. 12 ***

Figure 13 shows the designed beam optics, from point A to the beam dump. The quadrupole strengths in the section between the injection and dump chicanes, where the beam passes two times, were determined to match the beam optics at a lower energy. The optical functions were designed so that moderately small betatron functions were obtained throughout the beamline.

*** Fig. 13 ***

3. Subsystems of cERL

3.1 Electron gun and low-energy beam transport

3.1.1 Photocathode DC gun

Electron guns for ERL-based light sources should deliver electron beams with beam emittance under 1 mm-mrad and beam current of up to 100 mA. A photocathode DC

gun is one of the most promising candidates for such guns. This is supported by a successful operation of a 350-kV photocathode gun [33, 16] at the Cornell photoinjector. There, a high beam current of 65 mA and high beam brightness (90% normalized emittances of 0.3 mm-mrad with a bunch charge of 77 pC) were successfully demonstrated. To reduce the emittance growth due to space charge forces, the gun voltage is desired to be increased further.

A 500-kV photocathode DC gun, which is illustrated in Fig. 14, was adopted for the cERL. This electron gun was developed at the Japan Atomic Energy Agency (JAEA), and the generation of a 500-keV electron beam was successfully demonstrated [34]. This was achieved by solving two discharge problems. One was a discharge on the surface of an insulator ceramic which was caused by field-emitted electrons generated from a central stem electrode. To avoid such discharges, we employed a segmented insulator equipped with guard rings that protect the insulator against field emissions [35]. The other issue was a micro-discharge at the anode electrode or a vacuum chamber, which was triggered by the micro-particle transfer or field emission from the cathode electrode. We found that a larger acceleration gap, optimized mainly to reduce the surface electric field of the anode electrode, suppressed the micro-discharge events that accompanied gas desorption [36]. After the demonstration of 500-keV beams, the electron gun was transported and installed in the cERL.

*** Fig. 14 ***

The gun system is fully described in references [34–36]. A gallium arsenide (GaAs) wafer on a molybdenum puck was used as a photocathode. The wafer was atomic-hydrogen cleaned and transferred to the preparation chamber where cesium and oxygen were alternatively applied for NEA activation. The activated cathode was transferred to the cathode electrode in the gun chamber for beam generation. By laser light illumination (wavelength, 532 nm), the photoemission beam was produced and accelerated by a static electric field between the cathode and anode electrodes. The acceleration gap was surrounded by twenty of 0.4 m³/s non-evaporable getter (NEG) pumps (SAES getters, CapaciTorr D400-2), to reduce the amount of residual gas. A 0.2 m³/s ion pump (ULVAC, PST-200AU) was installed at the bottom of the gun chamber to pump noble gases and methane. The gun chamber and the electrodes were made of chemically polished titanium. A 1 m³/s turbo molecular pump was used during baking of the gun system. After the activation of the NEG pumps, the base pressure of the gun

chamber reached 7×10^{-10} Pa, and the pressure was measured using an extractor gauge.

A Cockcroft Walton high-voltage power supply (HVPS) was installed in a tank that was filled with a pressurized SF₆ gas. The output of the HVPS was connected to the gun high-voltage terminal via an output resistor. The output resistance was 0.1 GΩ for HV conditioning. Because an external resistor of 5 GΩ was connected to the segmented insulator in parallel, the output voltage of the HVPS was 510 kV when a voltage of 500 kV was applied to the insulator during HV conditioning.

3.1.2 The laser system

Beam emission from the gun is controlled by a laser beam which excites the photocathode. The drive laser system [37] controls various key parameters such as bunch charge, transverse beam profile, longitudinal pulse length, and the timing with respect to the rf acceleration. It also realizes several modes of beam operation, such as the burst mode used for machine tuning, together with the continuous wave (CW) mode. Emergency stop for machine protection was also implemented in the laser system.

The laser system is shown schematically in Fig. 15. Seed-laser pulses are produced using a commercial mode-locked pico-second laser (Time-Bandwidth Products, GE-100) which provides output power of 400 mW at a wavelength of 1064 nm with the pulse length of 10 ps in full width at half maximum (FWHM). The repetition rate of the laser pulses is 1.3 GHz, coinciding with the accelerator's rf frequency. The seed pulses can be synchronized to an external timing reference with the precision (stability) of 0.3 ps.

*** Fig. 15 ***

The seed-laser pulses are amplified up to the power of 50 W using a two-staged ytterbium-doped fiber amplifier. Since this is a high-average-power laser system, the thermal loads of components can affect the system's stability in the CW operation mode. The fiber-based system is advantageous for realizing a power-efficient system. The wavelength of the laser is converted into the second harmonic using a non-critical phase-matched lithium triborate (LBO) crystal. A typical laser beam produced by this system has an average power of 1 W, a wavelength of 532 nm, a repetition rate of 1.3 GHz, and the rms pulse length of 3 ps. The temporal profile of a laser pulse can be made quasi-rectangular by stacking multiple pulses. The transverse profile of a laser pulse can be made uniform-like by truncating a Gaussian distribution with a circular

aperture. The aperture is imaged on the cathode by a lens system in a laser transfer line.

3.1.3 Low-energy beam transport

In a low-energy beam transport (LEBT) between the gun and the injector cryomodule, there are a laser input chamber, a 1.3-GHz-frequency normal-conducting buncher cavity, two solenoid magnets, three steering magnets, two screen monitors, two stripline beam position monitors (BPMs), a cathode inspection mirror, and a Faraday cup [38]. The layout of the LEBT is shown in Fig. 16. Laser pulses are introduced into the gun through the laser input chamber. The angle of incidence with respect to the photocathode is $\sim 2^\circ$. By illuminating the laser pulses with the repetition frequency of 1.3 GHz, electron bunches are produced and are longitudinally compressed into an rms length of 2–3 ps using the buncher cavity [39]. The maximum rf voltage in the buncher cavity is 130 kV (for a particle with $\beta=1$) under usual operations.

*** Fig. 16 ***

Extremely low pressure is required in this section for keeping high quantum efficiency (QE) of the photocathode. For this purpose, both the pumping system and the vacuum chambers (including the buncher cavity) were designed very carefully. The pumping system consists of NEG pumps (two 2000 L/s pumps and five 400 L/s pumps for the hydrogen gas) and ion pumps (two 50 L/s pumps for the nitrogen gas). The laser input chamber was made of 0.2% beryllium copper alloy while the buncher cavity was made of oxygen-free high-conductivity copper (OFHC), both of which have very low outgassing rates. The input coupler of the buncher was designed for avoiding gas pockets in a junction.

The buncher cavity and the adjoining chambers were assembled in a clean room. The assembled chambers were installed in a local clean booth, which can reduce the contamination of dusts that potentially cause field emission of the injector SC cavities. After baking at 150 °C for 100 h, the vacuum pressure in the screen chamber 1 reached 2×10^{-9} Pa. After conditioning by the rf voltage of up to 190 kV, the pressure in the buncher cavity dropped below 3×10^{-9} Pa under high-power operation of up to 130 kV.

Both bunch charge and cathode QE were measured using the Faraday cup in the LEBT with a burst beam having a burst length of $\sim 1 \mu\text{s}$.

3.2 Superconducting cavity modules

3.2.1 Injector cryomodule

An injector cryomodule for the cERL is required to accelerate 10-mA-current CW electron beams from the kinetic energy of 500 keV to 5 MeV. An injector cryomodule containing three 2-cell cavities was designed [40] as shown in Fig. 17. The operating accelerating gradient (E_{acc}) of each 2-cell cavity is ~ 6.8 MV/m in the CW operation. Each cavity is driven by two input couplers to reduce the required rf-power handling capacity and to balance transverse momentum kicks due to input couplers. Each 2-cell cavity was dressed with a helium (He) jacket, which was made of titanium and maintained the temperature at 2 K. Magnetic shields were put inside the He jackets.

*** Fig. 17 ***

For damping higher order modes (HOMs), an HOM coupler scheme was chosen. Five loop-type HOM couplers were attached on both beam pipes of each cavity [41]. Rf feedthroughs for the HOM pick-up antennas were designed to provide efficient cooling, which is important for HOM couplers. As a frequency-tuning system, a slide-jack tuner equipped with a pair of piezo elements was attached at thick titanium base-plates.

An rf input coupler is the most critical component in high-power applications of superconducting cavities such as the cERL. A coaxial coupler, equipped with a warm (room temperature) single disk-type ceramic rf window with cooling water channels was used for the CW input couplers [42]. Since these couplers were assembled with cavities in a clean room before installation in the cryomodule (Fig. 18a), the couplers had to be as short as possible. Therefore, it is critical to efficiently remove both dynamic and static heat loads in the input couplers and in HOM extraction cables. The couplers were anchored to 5K He-reservoir panels, located on both sides of the 2-cell cavities, which also acted as thermal shields.

*** Fig. 18 ***

Assembly of the injector cryomodule was started in April, 2012, and the completed cryomodule was installed in the beamline [43], as shown in Fig. 18b. Then, cool-down tests for low- and high-rf power measurements were successfully performed before starting the beam commissioning. It was demonstrated that each coupler can transmit an rf power of 30–40 kW [42]. For the future beam-current upgrade to 100 mA, some improvement of its cooling mechanism is required.

3.2.2 The main linac cryomodule

Two 9-cell L-band superconducting cavities, which are cooled down to the temperature of 2 K by a helium refrigerator, were installed in the ML cryomodule [44]. The target accelerating gradient (E_{acc}) is ~ 15 MV/m, with the target unloaded Q-value of 10^{10} . The accelerating voltage (V_c) in each cavity is approximately given by $V_c[\text{MV}] = 1.038 \times E_{acc} [\text{MV/m}]$.

It is very important to strongly damp HOMs in the ML cavities, since the beam breakup instability due to HOMs is one of the key issues affecting the high-current operation of the future ERL-based light source. A 9-cell cavity, named KEK-ERL model-2 [45], was specially designed for the cERL ML. This cavity has a large iris diameter of 80 mm, and it allows us to strongly suppress its higher-order modes. A drawback of this cavity is a relatively high surface electric field in its iris region. Thus, suppressing the field emission is essential for its stable operation.

A schematic and a photograph of the ML cryomodule are shown in Figs. 19 and 20, respectively. In this cryomodule, the cavities were mounted with helium jackets, 5-K-temperature thermal shields, magnetic shields, and 80-K-temperature thermal shields. Two input couplers, two frequency tuners, and three HOM absorbers were also mounted in the cryomodule.

*** Fig. 19 ***

*** Fig. 20 ***

The input coupler [46] is coaxial type. It has double disk-type ceramic windows (cold (80 K) and warm (room temperature) windows), which can prevent dust contamination of the cavities. Variable external-Q, ranging from 1×10^7 to 4×10^7 , is available using bellows. The coupler is designed to transmit the rf power of 20 kW in the CW mode. The inside of the inner conductor is cooled by a flow of gaseous nitrogen.

To absorb the HOM power from the cavities, a beam-pipe-type absorber was developed [47]. In this absorber, a ferrite material, IB004 from the TDK Corporation, is used as an absorbing material. The ferrite material was bonded to a copper beam-pipe using the hot isostatic pressing (HIP) technique. The HOM absorbers are located on both sides of the cavity, and they can absorb the HOM power of more than 100 W per cavity. The absorbers are connected to 80-K-temperature thermal anchors.

Two types of frequency tuners, a mechanical slide-jack tuner [48] and a piezo tuner,

are used in the ML module. The mechanical tuner is used for coarse tuning. It can change the cavity length within 3 mm that corresponds to the change in the resonant frequency of 900 kHz. The other piezo tuner is used for precise tuning during beam operation, and it can change the resonant frequency by a few kHz.

3.3 RF source

A highly-stable cavity field is required for the ERL. The rf field for the future ERL-based light source should be stabilized within 0.01% (rms) in amplitude and 0.01° (rms) in phase, respectively. To achieve these requirements, stable high-power rf sources, stable rf-field feedback control, and tuner feedback control for high loaded-Q cavities are important.

Figure 21 shows the configuration of 1.3 GHz rf sources for the injector [49]. A buncher cavity is driven by an 8 kW solid state amplifier (SSA). The first SC cavity of the injector, INJSC1, is driven by a 25 kW klystron. The second and the third SC cavities, INJSC2 and INJSC3, are driven by a single 300 kW klystron, where the vector sum of picked-up signals from the cavities is stabilized. To adjust the phase between the two cavities, a phase shifter was installed along a waveguide to INJSC3. When the beam energy changes, a fine tuning of this phase shifter is necessary. In the future beam-current upgrade to 100 mA, each cavity will be driven by a separate klystron, and the 300 kW klystron (Toshiba, E37750) was developed for providing sufficient power under such situation.

*** Fig. 21 ***

In the ML, the beam loading is small due to energy recovery; however, potentially large input power due to cavity detuning by microphonics was a concern when designing the system. Based on high-power test results, we employed both 16 kW and 8 kW SSAs as the high-rf power sources for the first and the second ML cavities, MLSC1 and MLSC2, respectively. The advantages of SSAs are that their compactness, stability, and reliability. Figure 22 shows the installed SSAs.

*** Fig. 22 ***

A low-level RF (LLRF) system is based on the IQ digital feedback using field-programmable gate arrays (FPGAs). Micro-TCA digital feedback boards are employed for the rf-field control and for the resonant-frequency control by tuners [50–52]. Effects due to microphonics were satisfactorily suppressed. As a result, the rf

fields in each ML cavity was stabilized within 0.01% (rms) in amplitude and 0.01° (rms) in phase [53]. The high stability of the rf fields was confirmed using beams, as described in Sec. 5.4.1.

3.4 Cryogenic system

A 2-K-temperature superfluid helium cryogenic system [54] has been constructed for maintaining SC cavities in the injector and ML cryomodules at the temperature of 2 K. The cryogenic system consists mainly of a 4.4-K-temperature helium liquefier/refrigerator cold box (Sulzer, TCF200), two 2-K-temperature superfluid helium refrigerator cold boxes (Hitachi), high-performance transfer lines, and a helium-gas pumping system. Specifications of the system are summarized in Table 4.

*** Table 4 ***

Figures 23 and 24 show the layout and the flow diagram of the cryogenic system. Each cryomodule is connected to the 2-K-temperature refrigerator cold box that is located next to the cryomodule, by which the heat load to the 2-K-temperature system can be minimized. The other cryogenic components are installed outside the accelerator room, which allows to access them during the accelerator operation. The 2-K-temperature refrigerator cold boxes are connected to the 4.4-K-temperature refrigerator cold box by high-performance transfer lines via a 3000-L-volume vessel containing liquid helium.

*** Fig. 23 ***

*** Fig. 24 ***

Superfluid helium is produced by reducing the pressure of liquid helium using a helium pumping system, which consists of oil rotary pumps and mechanical boosters. For continuous production of superfluid helium, a Joule-Thomson (J-T) valve and a heat exchanger are employed in the 2-K-temperature refrigerator cold box. By exchanging heat between the supplied helium and the evaporated gas, the production rate of superfluid helium is improved. The lowest temperature that has been achieved in this system was 1.7 K, with only static heat loads.

The cryogenic system has been modified to improve its overall efficiency during long-term operation. To recover the enthalpy of the helium gas that is evaporated from the 5-K-temperature thermal shields in cryomodules, the evaporated gas is fed into a heat exchanger of the helium liquefier/refrigerator to cool down the inlet warm helium

gas. We have also replaced the vacuum pump oil with that for the helium compressor, which allows to return the helium gas directly to the compressor without using a purifier. However, it is still possible that air, water vapor, or some other contamination are introduced into the 2-K-temperature lines due to the low pressure of 3.1 kPa. This issue is presently the main issue of the 2-K-temperature cryogenic system.

3.5 Beam diagnostic system

Standard beam diagnostics, such as monitoring the beam position, beam profile, and beam loss, are important for early commissioning of the cERL. The beam monitors for the cERL are listed in Table 5, whereas a detailed description of design and initial results are given in [55].

*** Table 5 ***

For the main beam-position monitors (BPMs), we adopted a stripline-type BPM. A schematic of the BPM duct is shown in Fig. 25(a). The length of the electrodes was chosen to be 28.8 mm, for maximizing the sensitivity to the signal at 2.6 GHz, that is, the maximum repetition frequency of bunches in the ML section. The picked-up signals pass a bandpass filter having a central frequency of 1.3 GHz and a bandwidth of 20 MHz, and they are detected using a log-detection circuit with a wide dynamic range. A commercial high-speed data acquisition unit (Yokogawa, SL1000) with insulating input modules is employed as a digitizer.

*** Fig. 25 ***

Beam-position measurement in a section between the injection and dump chicanes, where the beam passes twice, is illustrated in Fig. 26 [55]. Using a burst beam with the burst length of ~ 1 μs , the head (or tail) of the BPM signal is produced only by the first (or the second) passage of the beam, due to the time lag of 0.3 μs in the recirculation loop. By gating these parts of the signal, we can separately detect the beam positions on the first and the second passages. In the case of CW beams, we can conduct similar measurements by introducing a bunch gap (missing bunches), with a gap length of ~ 1 μs .

*** Fig. 26 ***

A schematic view of the screen monitor (SCM) is shown in Fig. 25(b). Each SCM is equipped with a two-stage screen holder, which allows us to use two different screens according to the energy and intensity of the beam. The first screen is a 100- μm -thick

Ce:YAG scintillator. The beam incidence surface is coated with a 3-nm-thick aluminum layer to avoid damage due to charge-up. The second screen is a metal foil that will be used for generating an optical transition radiation (OTR) in the future accelerator study. When the SCM is not in use, it is concealed behind a cylindrical rf shield. The light emitted from the screen is extracted in the direction perpendicular to the beam axis, and then relayed to a charge coupled device (CCD) camera (Allied Vision Technologies, Prosilica GC650) via an optical window and a flat mirror.

Optical fibers are used as one of the fast beam-loss monitors (BLMs); these fibers are 10-m-long, and are installed along the vacuum chamber for covering the two arc sections. A photomultiplier tube (PMT; Hamamatsu, H10721-110) is attached at the upstream end of the fiber, and the data acquisition unit described above is used for analyzing the time structure of the output signal. This monitor is primarily used for estimating the amount of beam loss in each arc section. We also use fast BLMs, each of which comprises a CsI scintillator and a PMT, for local beam-loss detection and interlock.

We have also developed a bunch-length monitor [56] using coherent transition radiation and a Michelson interferometer to confirm the effect of bunch compression along the first arc section.

3.6 Magnet system

In the cERL, there are 8 main dipole magnets, 16 small dipole magnets, 65 quadrupole magnets, and 4 sextupole magnets [57], whereas those in the injector diagnostic line are not included. Those magnets were designed to fit future beam-energy upgrade to 125 MeV, and are currently operated at considerably smaller fields than the maximum ones. The main dipole magnets, used in the two arc sections, are trapezoidal-shaped sector ones with the bending radius of 1 m and the bending angle of 45° each. The magnetic core consists of laminations of silicon steel. There are six types of small bending magnets, which are used for merger, injection and dump chicanes, a path-length control chicane, and for path-length control steering magnets. The magnetic cores of the small dipole magnets are made of electromagnetic soft iron.

Newly fabricated fifty seven quadrupole magnets are classified into two types with the same core shape but with different core lengths. The thinner quadrupoles (core length: 100 mm) are used for the low-energy beamline while the thicker ones (core

length: 200 mm) are used for the high-energy beamline. The magnetic core consists of laminations of silicon steel.

All sextupole magnets are identical and used to conduct the bunch compression and decompression for generating coherent THz radiation [58]. All the quadrupole magnets can work as horizontal and vertical steering magnets by using their sub-coils. All the main and small dipole magnets have sub-coils for horizontal steering. The sextupole magnets can generate a vertical dipole field for the horizontal steering and a skew quadrupole field for the vertical dispersion correction by their sub-coils.

These magnets and their girders were installed, and aligned using a laser tracker and a tilting level by referring 40 surveying references on the inner walls of the accelerator room. The magnets were aligned within positional and angular deviations of ~ 0.25 mm and ~ 0.1 mrad, respectively. The modest position accuracy was due to disassembling and reassembling the upper parts of the magnets after the alignment.

The magnets are excited by power supplies that suit a beam energy of 35 MeV. The eight main dipole magnets are connected in series, and are excited by a switching-type power supply with 100 A @ 40 V output rating [59]. On the other hand, all of the quadrupole magnets, including the sub-coils, are individually powered by using linear amplifier power supplies with ± 5 A @ ± 60 V output rating. In each chicane, the main coils of the chicane magnets are connected in series and excited by a 10 A power supply. Sub-coils are powered individually by 5 A power supplies for fine adjustment. Each path-length-control steering magnet is excited by a 10 A power supply. Ripples of the power supplies are less than 40 ppm of the rated output currents.

3.7 Vacuum system

The cERL vacuum system was designed to achieve pressures below 1×10^{-7} Pa along the beam path. This low pressure is primarily requested from a beam-loss rate due to beam-gas scattering, and secondly from ion trapping or fast ion instability. With the assumed pressure of 1×10^{-7} Pa, the beam-loss ratio due to the beam-gas scattering is below 10^{-7} [23] for the beam current of 100 mA and beam energy of 35 MeV, that is, even after a beam-current upgrade.

Beam tubes are mostly fabricated of 316L stainless steel with the inside diameter of 50 mm in straight sections and a 40-mm-high and 70-mm-wide oblong octagon in arc sections (Fig. 27). The entire vacuum system is pumped down by 64 NEG pumps and

51 sputter ion pumps (SIPs), and the pressures are monitored by 51 cold cathode gauges (CCGs). The CCGs should be located sufficiently far away from the beam, or be magnetically shielded, to prevent their magnetic fields from affecting low-energy beams. After the bakeout of the vacuum components and the activation of the NEG pumps, the pressures reached 10^{-8} Pa.

*** Fig. 27 ***

In the sections adjacent to the superconducting cavities, dust-free vacuum is required to exploit their full performances. Prior to the installation, all of the vacuum components were carefully blown using a compressed-air jet in a class-10 clean room, and then assembled in a mobile clean booth. Beam tubes installed inside the quadrupole magnets were coated with NEG thin films, intended to reduce gas condensation on the cavity's cryo-surfaces.

In order to accommodate high intensity, low emittance, and short bunch electron beams, low-impedance vacuum components that can suppress wake-field excitation are required. We therefore developed vacuum flanges devoid of gap or step structure [60] and retractable screen monitors with rf shielding [55]. The special flange is capable of attaining a pressure of 10^{-9} Pa after bakeout, and no vacuum leak was detected at over 160 flange joints during the machine construction.

A movable Faraday cup is installed right after the second arc. The body of the Faraday cup is a 150-mm-long and water-cooled copper block, which can measure the bunch charge of up to 125-MeV-energy and 10-nA-current beams before re-entering the main cavity. The body is concealed behind an rf shield while not in use. At the end of the beam path, the decelerated beams are absorbed in the main beam dump, which also functions as a Faraday cup. The present main beam dump was designed to accommodate a beam current of 10 mA. The body is a 400-mm-long and water-cooled GlidCop cylinder with a corn-shaped absorbing surface.

3.8 Control system

The control system was designed to accommodate reliable access to every device of the cEERL and to support various accelerator studies and tuning with a user-friendly interface. All devices and computers are connected to a local control network, as shown in Fig. 28. For the central software environment, we adopted an open-source software, the Experimental Physics and Industrial Control System (EPICS) [61], since it can

provide a sophisticated and reliable platform from the active EPICS-user community. Because the EPICS software is used in other accelerators, such as Super-KEKB [62] and the Photon Factory [63], it allows us to rapidly develop necessary software by making use of available resources.

*** Fig. 28 ***

Devices under control are accessed from input output controllers (IOCs) using the channel access protocol. The IOCs are primarily based on a programmable logic controller (Yokogawa, F3RP61 CPU unit) running in the Linux operating system. Six server computers are used to process high-level applications, simulations, and data archives, as well as to provide gateway and web servers. Graphical user interfaces were developed using an EPICS toolkit, the Control System Studio (CSS). It allows us to develop the operator interface (OPI), alarm display and management, and interface with archived data.

The cERL control room is located beside the hall of the ERL development building. In a room of 14.4 m × 6.3 m, ~10 personal computers are installed for operators' console. The control room is also equipped with components of the safety system, such as status display, console, an emergency switch, display of surveillance cameras, and a loudspeaker mike. An electric log system, Zlog [64], is used for logging operations.

3.9 Radiation shield and safety system

The cERL is built in an existing building that was used for high-energy physics experiments. Since the cERL is a high-intensity linac that is built on the ground, its radiation shield is desired to be as thick as possible. Considering a load capacity of the floor, which is estimated to be 17 tons/m², we designed the radiation shield (the cERL accelerator room) as shown in Fig. 29. It comprises many blocks of reinforced concrete. Thicknesses of side and top walls were determined to be 1.5 m and 1 m, respectively.

*** Fig. 29 ***

With the designed shield, beam losses along the recirculation loop should be kept considerably small. If a fraction of a 35-MeV beam is lost at a certain point of the beamline, a tolerable amount of beam loss is roughly 10 nA, which corresponds to a beam-loss ratio of 10⁻⁶ for the beam current of 10 mA. A local shield, arranged nearby an anticipated beam-loss point, can increase the tolerable beam loss to 100 nA or make it even higher. To achieve such small beam losses, we installed five beam collimators

[65] as shown in Fig. 30. Each collimator has four plungers of water-cooled copper, which are inserted in both horizontal and vertical directions. Beam halos or tails are mainly eliminated by two collimators, COL1 and COL2, located in the low-energy (5 MeV) section. The remaining beam halos are also eliminated by the other three collimators, COL3 to COL5. Each collimator is locally shielded with a 20-mm-thick lead jacket and lead blocks. With current local shields, tolerable amounts of beam losses are 1 μA and 10 μA (at 6 MeV) at the collimators of COL1 and COL2, respectively, and 50–100 nA (at 26 MeV) at the collimators of COL3 to COL5.

*** Fig. 30 ***

When a large beam loss happens during the accelerator operation, the beam production is immediately interrupted by cutting drive-laser pulses to the gun. For this purpose, we installed three types of beam-loss or radiation monitors: 1) fast beam-loss monitors [55] that were described in Sec. 3.5, 2) radiation monitors (Hitachi Aloka Medical, MAR-782) inside the accelerator room, and 3) radiation monitors outside the accelerator room. These monitors were arranged as shown in Fig. 30. Using the fast loss monitors, we can stop the beam within 10 μs while the other loss or radiation monitors are used as a backup. Beams are also stopped when there is a problem with any of the accelerator components, such as a trip in an rf power. Such an interlocking logic was implemented in a machine-mode system (MMS). Ordinary safety functions, such as a door interlock, emergency-stop switches, personal keys, status indicators, personnel evacuation process, and a beam-power limiter, were also implemented in a personnel protection system (PPS).

4. Progress of construction

4.1 Construction

The progress of the cERL construction is summarized in Table 6. Both the injector and injector-diagnostic line were commissioned during the period from April to June, 2013 [38]. During this period, electron beams were successfully accelerated up to the total energy of 6.1 MeV. Typical operational parameters were: a gun cathode voltage of 390 kV and accelerating gradients of 6.8–7.2 MV/m in the injector cavities. At a bunch charge of 7.7 pC, normalized emittances of 0.49–0.90 mm·mrad were measured [38] in the injector-diagnostic line.

*** Table 6 ***

Before the installation of the recirculation loop, we decided the target beam energy to be 19.9 MeV due to the reasons described in Sec. 4.2, and determined the positions of the magnets that would yield optimal circumference for the beam energy of 20 MeV. From July to November, 2013, we installed the components of the recirculation loop [66]. Figure 31 shows the entire layout of the cERL. The cERL is shown in Fig. 32.

*** Fig. 31 ***

*** Fig. 32 ***

4.2 High-voltage or high-power tests of DC gun and SC cavities

The photocathode DC gun was conditioned up to a high voltage of 550 kV [34] at the JAEA site, and then, transported to KEK and installed. During the high-voltage testing at KEK, however, we found that the maximum voltage of the gun was limited to 400 kV, due to discharges [67]. The discharges occurred in two (top and bottom) segments of the insulator ceramic, both of which had some contamination. We placed short bars between the electrodes of failed segments, and decided to operate the gun at the cathode voltage of 390 kV.

After installing the injector cryomodule, the three 2-cell SC cavities of the injector were cooled down and tested with high rf power [68]. Each cavity was conditioned up to the accelerating gradient of 15 MV/m under pulsed rf power (pulse length: 50 ms, repetition rate: 2 Hz). Then, each cavity was conditioned up to the accelerating gradient of 8 MV/m under CW rf power. No radiation associated with field emission was observed up to 8 MV/m.

After installing the ML cryomodule, the two 9-cell SC cavities (ML-1 and ML-2) were cooled down and tested with high rf power [69]. Both cavities were successfully tested up to the accelerating gradient of 15.4 MV/m under CW operation. However, field emissions emerged above the accelerating gradient of ~ 8 MV/m. As a result, unloaded Q values became lower than 10^{10} at field gradients above 10 MV/m. Under the vertical test of these cavities, which was conducted before the module assembly, the two cavities demonstrated excellent performances: unloaded Q values were higher than 10^{10} at 20 MV/m, and field emission onsets of 14 MV/m and 22 MV/m, respectively. Then, the field emissions were supposed to be due to contamination by dust particles during the module assembly. Due to the tight construction schedule and other reasons, we decided to start commissioning with these ML cavities. The accelerating gradient of

8.19 MV/m (accelerating voltage of 8.5 MV in each cavity) was chosen for standard operation.

Considering both the above-mentioned limitation of accelerating gradients and the restriction of momentum ratio, $p_i/p_r \leq 1/6$, the total beam energies of the injector and the recirculation loop were determined to be 2.9 MeV and 19.9 MeV, respectively, for the initial commissioning.

5. Commissioning of cERL

5.1 First beam commissioning

The first commissioning of the recirculation loop started in December, 2013. The accelerator parameters for these operations are given in Table 7 while the designed beam optics of the injector is shown in Fig. 33. Beam tuning was conducted under a burst mode, and typical parameters were: bunch charge of a few tens of femto coulombs (fC), burst lengths of 0.1–1.2 μ s, and burst repetition rate of 5 Hz. The space charge effect is negligible at these low-bunch charges. The photocathode was excited using laser pulses with the pulse length of ~ 3 ps (rms), and the buncher cavity was tentatively turned off. With an estimated laser-spot diameter of 1.1 mm (or equivalently, an rms size of 0.275 mm for uniform distribution) at the photocathode surface, normalized beam emittance of 0.13 mm·mrad is expected from Eq. (1) at the photocathode.

*** Fig. 33 ***

*** Table 7 ***

During the commissioning, transverse beam profiles and central orbit were tuned using screen monitors. Figure 34 shows the layout of the beam monitors and some other components. In the first several days, an injected beam was successfully accelerated up to ~ 20 MeV, with a small energy spread. The beam energy was measured using the bending magnet of the first arc. The beam was then transported down to the entrance to the dump chicane. At this time, we found that ambient magnetic fields affected the beam. Thus, we shielded the injected beam from fringe fields of the chicane magnets, and installed magnetic shields [70] in some of the CCGs.

*** Fig. 34 ***

Beam-position measurements on the second passage in a section between the injection and dump chicanes were performed using the method described in Sec. 3.5. Orbit correction on the second passage in this section was conducted using correctors

that were located before the injection chicane. To recover the beam energy ideally, the path length of the loop was adjusted so that the particle momentum became minimum at the dump line. An example of this adjustment is shown in Fig. 35, where the horizontal beam positions (corresponding to the particle momentum) at the dump line are shown as a function of the path-length change.

*** Fig. 35 ***

After tuning the beam orbit and the path length, together with removing unwanted fields, the beam was decelerated to an energy that was almost equal to the injection energy, and the beam was successfully transported to the main dump without significant beam loss on February 6, 2014 [66].

To increase an average beam current, it is important to reduce the beam loss. To this end, the bunch length was compressed with the buncher cavity, which can reduce the beam loss due to bunch tails. The optics matching of the transverse beam profile was also performed. After these tuning steps, an average beam current of 6.5 μA was successfully recirculated in the CW mode on March 14, 2014, without significant beam loss.

5.2 Confirmation of energy recovery

To confirm the energy recovery in the ML, we measured the difference between the input and reflected rf-power, ($P_{\text{in}} - P_{\text{ref}}$), in each ML cavity, for high-current CW mode beams. Figure 36 shows an experimental result where the power difference, ($P_{\text{in}} - P_{\text{ref}}$), was measured under two operation modes that were “beam loading” and “energy recovery” modes. Note that the variation in the power difference, $\Delta(P_{\text{in}} - P_{\text{ref}})$, is shown in Fig. 36 while subtracting an offset; the offset was determined so that $\Delta(P_{\text{in}} - P_{\text{ref}}) = 0$ without beam currents. In the “beam loading” mode, the beam was accelerated in an upstream ML cavity, and then decelerated in the other downstream cavity. Then, the beam went directly to the dump without beam recirculation. In the other “energy recovery” mode, the beam was accelerated in both ML cavities, transported through the loop, and decelerated in the ML cavities, and went to the dump, in the same manner as the normal ERL operation. According to the result in Fig. 36, the power difference $\Delta(P_{\text{in}} - P_{\text{ref}})$ under the beam-loading mode increased in the upstream cavity while it decreased in the downstream cavity, when the beam current increased up to $\sim 6.5 \mu\text{A}$. This indicates positive and negative beam loadings in each cavity. In the energy recovery

mode, on the other hand, the power difference did not depend on the beam current, which indicated that the beam loading was almost zero. This experiment clearly demonstrated the energy recovery in the ML cavities.

*** Fig. 36 ***

5.3 Optics measurements and tuning

We conducted optics measurements and tuning over the range from the gun to the beam dump. At first, we investigated [71] the transverse focusing effect of the photocathode DC gun due to a static electric field, which can affect downstream beam optics. For this purpose, we scanned the position of the laser spot on the photocathode, and measured the response of the beam central position at the downstream screen monitor. Because the focusing effect sensitively depends on the detail dimensions of the cathode electrode, the measured response did not agree with the one from the initial simulation. Thus, we adapted our model of the cathode electrode so that the simulation reproduced our measured response. This updated model was used in subsequent simulations.

In the next step, we investigated the beam optics inside the injector SC cavities [72]. We scanned an rf phase of each cavity, and measured the response of the beam position on the screen monitor that was located behind the injector. If the beam passes through the electromagnetic center of the cavity, the response does not depend on the rf phase. Using this behavior, we estimated the electromagnetic center of each cavity from the measured response. Note that the injector cavities INJSC2 and 3 are driven by a single rf source, and these cavities were investigated together. After that, we measured the relation between the emittance growth and the orbit offset inside the cavity. Finally, we minimized the emittance growth inside the injector cavities by adjusting the beam orbit.

After tuning the injector, we studied the beam optics from the merger to the beam dump using a quadrupole-scan (Q-scan) method. In this method, we scanned the strength of the target quadrupole magnet and measured the responses of horizontal and vertical beam sizes on the downstream screen monitor. We conducted this measurement at several locations in the loop. Initially measured responses did not agree with the results of simulations, which suggested that the beam optics differed from the designed one. The possible causes of this discrepancy were the hysteresis of the magnets, the effect of input-coupler kicks in the injector cavities, or other effects. We found that at

least the magnetic hysteresis significantly affected the beam optics because the magnets were used at considerably smaller fields than the designed maximum ones. Thus, we took care to standardize the magnets before and after every optics tuning. In addition, both the bending and quadrupole magnets exhibited significant residual fields after the standardization, and we compensated these residual fields by adding excitation current offsets. After taking these measures, the beam optics became more reproducible.

To bring the beam optics closer to the designed one, we matched [73] the optical functions using Q-scan measurements. In this method, five adjoining quadrupole magnets were used, where the most downstream quadrupole was used for Q-scan measurements. We conducted several Q-scan measurements by slightly changing the strengths of the other four quadrupoles one by one. Using the measured responses of the four quadrupoles in Q-scan measurements, we adjusted the strengths of the four quadrupoles so that the results of the Q-scan measurements became closer to the one expected from the designed optics. Using this method, we matched the beam optics at seven locations (matching points) in the recirculation loop. As a result, the optical functions became closer to the designed ones.

The dispersion functions in the recirculation loop were measured [74] using beam position monitors while changing the accelerating voltage of the ML, which gave a momentum deviation of approximately -1%. The horizontal dispersion (η_x) was then corrected by tuning two triplets in each arc. Especially, η_x at the center of the arc was adjusted to be 0.24 m for the isochronous condition, as described in Sec. 2.3, and that in the straight sections was corrected to be approximately zero for the achromatic condition. Figure 37 shows the measured dispersion functions after the correction, compared with the designed ones.

*** Fig. 37 ***

5.4 Measurement of beam parameters

5.4.1 Momentum spread and jitter

The momentum spread of the beam was measured at a screen monitor, SCM-15, that was located at the center of the first arc (Fig. 34). To enhance the dispersion function at the screen monitor, the triplet quadrupoles of the first arc were turned off, which resulted in the measured horizontal dispersion of approximately -2.2 m at the screen.

The pulse length of the cathode excitation laser was ~ 3 ps (rms), the rf voltage in the buncher cavity was ~ 30 kV, and the bunch charge was ~ 60 fC.

The measured horizontal rms beam size was $310 \mu\text{m}$, which corresponded to ~ 5 pixels of the CCD camera of the screen monitor. Considering an estimated contribution of beam emittance, $(\epsilon_x \beta_x)^{1/2} \sim 146 \mu\text{m}$, we obtained an rms momentum spread (σ_p/p) of approximately 1.2×10^{-4} . We thus confirmed that the momentum spread was very small at the first arc. Note that both the space charge and the CSR effects were negligible due to a low bunch charge. From the GPT simulation, the momentum spread was estimated to be 5.0×10^{-5} at the exit from the ML for a low bunch charge. The measured momentum spread was roughly two times this estimation.

The jitter in the beam momentum was also measured using the same setup as that used for measuring the momentum spread. The horizontal positions of the beam (that is, positions of the distribution peaks) were measured with the screen monitor, SCM-15, at the sampling rate of 5 Hz. The burst beam was used with the following parameters: the burst length was $\sim 1 \mu\text{s}$, the repetition rate was 5 Hz, and the bunch charge was ~ 20 fC. Assuming that the position jitter was mainly caused by the momentum jitter, the momentum jitter was deduced as shown in Fig. 38. Corresponding to a single pixel of CCD camera, the resolution of the momentum deviation $(\Delta p/p)$ measurement was $\sim 2.6 \times 10^{-5}$. From Fig. 38, we obtained the relative momentum jitter of approximately 6.4×10^{-5} (rms) during the measured period of 50 min. Such a low momentum jitter was successfully achieved due to a high field stability of SC cavities, as mentioned in Sec. 3.3.

*** Fig. 38 ***

5.4.2 Transverse emittance

The normalized transverse emittance was measured for a low bunch charge of ~ 14 fC, for which the space charge effect was negligible. The measurements were based on the quadrupole-scan method using a quadrupole magnet and a screen monitor, and were performed at four locations, A to D, as shown in Fig. 39. To conduct precise measurements, the minimum beam size at the waist condition should be larger than the spatial resolution of the screen monitor. This requirement was satisfied by selecting a screen monitor that was located sufficiently far away from the quadrupole magnet to be scanned. In addition, the camera gain and the attenuation filter arranged just before the

camera lens were optimized to avoid the CCD saturation even at the waist condition for each screen monitor. The exposure time of the camera was set to 100 μ s, which was sufficiently short for observing individual burst beams.

*** Fig. 39 ***

A typical result of the Q-scan measurement, conducted at location C, is shown in Fig. 40. The horizontal and vertical normalized-emittances were obtained by fitting the Q-scan data with roots of quadratic functions using the weighted least squares method [75]. Measurement errors were deduced from the fitting errors of coefficients in a polynomial of K . The measurements are summarized in Table 8. For a low bunch charge, the normalized emittances of approximately 0.14 mm·mrad were obtained at the four locations in both horizontal and vertical directions. This result was consistent with the estimated normalized emittance of 0.13 mm·mrad at the photocathode (Sec. 5.1).

*** Fig. 40 ***

*** Table 8 ***

6. Discussion

We discuss the present performance of the cERL in the context of our R&D efforts to develop an ERL-based x-ray source. The photocathode DC gun was successfully commissioned at the cathode voltage of 390 kV, that is, the highest operational voltage among similar guns. The gun produced low-emittance (0.49–0.90 mm·mrad at 7.7 pC/bunch) beams, as reported in [38]. It delivered beams for 1387 hours during the period from April 2013 to March 2016, without any discharges. These results demonstrate that our photocathode DC gun is suitable for practical use in the ERL x-ray source. An issue that remains is to demonstrate a long cathode lifetime under high average current (≥ 10 mA), although it was demonstrated [33] at the other facility.

The injector cryomodule for two-cell SC cavities demonstrated the CW-rf operation at the accelerating gradient of 7 MV/m and at the transmitted power reaching 30–40 kW/coupler. With this module, an ERL injector of 5-MeV-energy, 10-mA-current class is buildable. An injector of higher energy, or higher current, is available if we use two or three modules. The beam current will also be increased up to 100 mA with a single module if we reinforce the cooling mechanism in our input couplers, by which the transmitted rf power will be increased to about 100 kW/coupler. To reduce dynamic losses, reinforced cooling of our HOM couplers is also desirable.

The ML cryomodule, equipped with 9-cell SC cavities, HOM absorbers, and precise frequency tuners, was commissioned. During the cERL operation, two SC cavities worked stably in the CW-rf mode at the accelerating gradient of ~ 8.2 MV/m. Although the achieved operational gradient was lower than our target of 15 MV/m, the basic designs of cavity and cryostat were demonstrated. To construct the ERL x-ray source, it is necessary to increase the gradient to ~ 15 MV/m. We consider that the low gradient was caused by the dust contamination during the module's assembly; if so, this can be resolved by improving the module assembly process. This effort is in progress using a new horizontal test stand. For constructing the ERL x-ray source, a test of the ML module under a high average current (≥ 10 mA) is also necessary for confirming the robustness of HOM absorbers together with a sufficient margin of the BBU threshold current.

Successful stabilization of rf fields in the ML cavities, that is, within 0.01% (amplitude; rms) and 0.01° (phase; rms), was demonstrated using an advanced low-level rf system. This fits the requirement for the ML of the ERL x-ray source.

The cERL was constructed by integrating the above-mentioned critical components. We demonstrated the recirculation of CW beams while recovering beam energy in the ML. It means that all critical components worked together in a real accelerator environment. For a low bunch charge (under 100 fC/bunch), we demonstrated high beam quality such as the normalized transverse emittance of ~ 0.14 mm·mrad, the momentum spread of $\sim 1.2 \times 10^{-4}$ (rms), and the momentum jitter of $\sim 6 \times 10^{-5}$, at the recirculation loop.

The future 3-GeV ERL [12] requires the normalized emittance of ~ 0.1 mm·mrad (at 7.7 pC/bunch) and the momentum spread of $\sim 2 \times 10^{-4}$ (rms), including the momentum jitter, at the bunch length of ~ 2 ps (rms). The beam quality at the cERL almost meets these requirements for low bunch charges, but it should be demonstrated for higher charges of 7.7–77 pC/bunch. Under the low-bunch-charge operation of the cERL, the photocathode was excited by short (3 ps in rms) laser pulses. Under higher charges, the photocathode is excited by long (about 16–32 ps in FWHM) laser pulses, with each pulse comprising a stack of the short laser pulses. Production of such long-pulse bunches was demonstrated at the cERL. We are conducting studies of acceleration and compression of these bunches while preserving small beam emittance. We have some issues to be studied for controlling space-charge and non-linear forces under high bunch

charges.

Concerning high beam currents, the cERL demonstrated the recirculation of an average beam current of ~ 0.9 mA, as was briefly reported in [65]. A higher beam current of at least 10 mA, with a beam-loss ratio below 10^{-7} , should be demonstrated further. There remain other issues such as understanding the formation of beam halos, beam diagnostics for high average currents, and demonstration of high beam stability. The successful commissioning of the cERL provides a solid basis for future full demonstration of the ERL x-ray source, as well as for other applications of ERL.

7. Conclusions

To demonstrate the critical technology for the ERL-based light source, the compact ERL was constructed and commissioned. Based on the photocathode DC gun and superconducting rf technology, the cERL was designed to be capable of recirculating low emittance (≤ 1 mm-mrad) and high average-current (≥ 10 mA) electron beams while recovering beam energy. During the commissioning, the key components worked reliably. For low bunch charges (< 100 fC), we demonstrated the production and recirculation of high-quality beams with: the normalized transverse emittance of approximately 0.14 mm-mrad, the momentum spread of approximately 1.2×10^{-4} (rms), and the beam energy of 20 MeV. Energy recovery in the ML cavities was demonstrated with high-average-current CW beams. The successful commissioning of the cERL provides a basis for future full demonstration for the ERL-based light source.

Acknowledgments

The authors would like to thank the following people who cooperated, or helped us, to design, construct, or commission the compact ERL. Toshiya Muto (KEK and Tohoku University), Shunya Matsuba (Hiroshima University and JAEA), and Hokuto Iijima (JAEA and Hiroshima University) contributed to developing the photocathode DC electron gun. Hitoshi Hayano, Akira Yamamoto, Motoaki Sawabe, and other members of Superconducting RF Test Facility (STF) of KEK, supported the processing and vertical tests of our SC cavities. Masahiro Adachi, Hiroyuki Honma, Xiuguang Jin, Ryuko Kato, Takayuki Kubo, Taro Konomi, Shuji Matsumoto, Toshihiro Matsumoto, Hiroshi Miyauchi, Katsumi Nakao, Tetsuo Shidara, Tatsuro Shioya, Toshihiro Tahara, Hiroyuki Takaki, Makoto Tobiya, Kimichika Tsuchiya, Naoto Yamamoto,

Yasuchika Yamamoto, Yoshiharu Yano, and Mitsuo Yoshida (all from KEK) cooperated in the construction and/or operation of the cERL. Yohei Kobayashi (AIST* and ISSP**), Dai Yoshitomi (AIST), Isao Ito (ISSP), and Taisuke Kawasaki (ISSP) cooperated in the laser development. Takeshi Shiraga (ISSP) and Yuji Seimiya (KEK and Hiroshima University) collaborated on beam dynamics simulations. Atsushi Ishii (ISSP and KEK) worked on the structural analysis of magnet girders. Hwang Ji-Gwang (Kyungpook National University and Korea Institute of Radiological & Medical Sciences) and Alessandra Valloni (CERN) joined the accelerator physics study. We had fruitful discussions on the cERL design with Masahiro Katoh (Institute for Molecular Science), Hirofumi Hanaki (JASRI), Hiromitsu Tomizawa (JASRI), Masanori Kobayashi (KEK), Toshio Kasuga (KEK), Satoshi Ohsawa (KEK), Toshiyuki Mitsuhashi (KEK), and Toshiyuki Ozaki (KEK). Tsutomu Nakanishi (Nagoya University, deceased) provided valuable advice on the photocathode gun. Yoshikazu Takeda, Makoto Kuwahara, and Toru Ujihara (all from Nagoya University) cooperated on the photocathode R&D effort. Hiroki Kurisu (Yamaguchi University) helped us to design an extremely-high vacuum chamber. Steve Benson, Kevin Jordan, Vaclav Vylet, Pavel Evtushenko, Carlos Hernandez-Garcia, Christopher Tennant, Robert Legg, and Daniel Sexton (all from Thomas Jefferson National Accelerator Facility) shared with us their valuable experience of operating the IR-FEL machine. Bruce Dunham (Cornell University) and Jochen Teichert (HZDR) also provided us useful information and advice. Yoshihito Namito, Taichi Miura, Yuji Kishimoto, Ken-ichi Hozumi, Akihiro Toyoda, Takahiro Oyama, and Seiji Nagaguro (all from KEK) managed radioactive issues. Masaharu Ieiri, Yohji Katoh, and Erina Hirose (all from KEK) cleared the East Counter Hall for cERL construction. Some members of Hitachi Plant Mechanics Co. Ltd., Nippon Advanced Technology Co. Ltd., East Japan Institute of Technology Co. Ltd., Mitsubishi Electric System & Service Engineering Co. Ltd., and K-vac Co., helped us with constructing and/or operating the cERL. Finally, we acknowledge continuous encouragement given by Yukihide Kamiya, Osamu Shimomura, Soichi Wakatsuki, Katsunobu Oide, Shinichi Adachi, and Tadashi Matsushita (all from KEK). This work was partly supported by a Government (MEXT) Subsidy for Strengthening Nuclear Security, and by the Quantum Beam Technology Program of Japanese Ministry of Education, Culture, Sports, Science and Technology (MEXT).

* AIST: National Institute of Advanced Industrial Science and Technology

** ISSP: Institute for Solid State Physics, the University of Tokyo

References

- [1] M. Tigner, *Nuovo Cimento* 37 (1965) 1228.
- [2] G.R. Neil et al., *Phys. Rev. Lett.* 84 (2000) 662.
- [3] R. Hajima, T. Shizuma, M. Sawamura, R. Nagai, N. Nishimori, N. Kikuzawa, E.J. Minehara, *Nuclear Instruments and Methods in Physics Research A* 507 (2003) 115.
- [4] N.A. Vinokurov et al., *Commissioning Results with Multi-Pass ERL*, in: *Proceedings of the 23rd Particle Accelerator Conference (PAC2009)*, Vancouver, Canada, May 408, 2009, MO4PBI02.
- [5] Sol M. Gruner, D. Bilderback, I. Bazarov, K. Finkelstein, G. Krafft, L. Merminga, H. Padamsee, Q. Shen, C. Sinclair, M. Tigner, *Rev. Sci. Instrum.* 73 (2002) 1402.
- [6] I. Ben-Zvi, Ya. Derbenev, V.N. Litvinenko, L. Merminga, *Nuclear Instruments and Methods in Physics Research A* 557 (2006) 28.
- [7] O. Brüning, *Overview of the LHeC Design Study at CERN*, in: *Proceedings of the fourth International Particle Accelerator Conference (IPAC'13)*, Shanghai, China, May 12-17, 2013, MOZB201.
- [8] R. Hajima, T. Hayakawa, N. Kikuzawa, E. Minehara, *J. Nucl. Sci. Tech.*, 45 (2008) 441.
- [9] G.H. Hoffstaetter, Sol M. Gruner, M. Tigner (eds.), *Cornell Energy Recovery Linac Science Case and Project Definition Design Report*,
<http://www.classe.cornell.edu/rsrc/Home/Research/ERL/PDDR/PDDR.pdf>
- [10] G.N. Kulipanov, Ya.V. Getmanov, O.A. Shevchenko, A.N. Skrinsky, A.G. Tribendis, V.N. Volkov, *Multiturn ERL x-ray Source (MARS) Feasibility Study*, in: *Proceedings of the 50th ICFA Advanced Beam Dynamics Workshop on Energy Recovery Linacs (ERL2011)*, Tsukuba, Japan, Oct. 16-21, 2011, WG2013.
- [11] T. Atkinson, A. V. Bondarenko, A. N. Matveenko, Y. Petenev, *The Femto-Science Factory: A Multi-turn ERL Based Light Source*, in: *Proceedings of the 56th ICFA Advanced Beam Dynamics Workshop on Energy Recovery Linacs (ERL2015)*, Stony Brook, USA, June 7-12, 2015, MOPBTH003.
- [12] *Energy Recovery Linac Conceptual Design Report*, KEK Report 2012-4 (2012),
<http://ccdb5fs.kek.jp/tiff/2012/1224/1224004.pdf>
- [13] N. Nakamura, *Review of ERL Projects at KEK and Around the World*, in: *Proceedings of the third International Particle Accelerator Conference (IPAC'12)*, New Orleans, USA, May 20-25, 2012, TUXB02.

- [14] K.-J. Kim, Y. Shvyd'ko, S. Reiche, Phys. Rev. Lett. 100 (2008) 244802.
- [15] S. Benson, M. Borland, D.R. Douglas, D. Dowell, C. Hernandez-Garcia, D. Kayran, G.A. Krafft, R. Legg, E. Moog, T. Obina, R. Rimmer, V. Yakimenko, Nuclear Instruments and Methods in Physics Research A 637 (2011) 1.
- [16] C. Gulliford, A. Bartnik, I. Bazarov, L. Cultrera, J. Dobbins, B. Dunham, F. Gonzalez, S. Karkare, H. Lee, H. Li, Y. Li, X. Liu, J. Maxson, C. Nguyen, K. Smolenski, Z. Zhao, Phys. Rev. ST Accel. Beams 16 (2013) 073401.
- [17] Y. Saveliev et al., Recent Developments on ALICE (Accelerators and Lasers in Combined Experiments) at Daresbury Laboratory, in: Proceedings of the first International Particle Accelerator Conference (IPAC'10), Kyoto, Japan, May 23-28, 2010, TUPE096.
- [18] S. Sakanaka et al., Recent Progress and Operational Status of the Compact ERL at KEK, in: Proceedings of the sixth International Particle Accelerator Conference (IPAC'15), Richmond, USA, May 3-9, 2015, TUBC1.
- [19] D. Kayran et al., Status and Commissioning Results of the R&D ERL at BNL, in: Proceedings of the 56th ICFA Advanced Beam Dynamics Workshop on Energy Recovery Linacs (ERL2015), Stony Brook, USA, June 7-12, 2015, MOPDTH014.
- [20] M. Abo-Bakr et al., Progress Report of the Berlin Energy Recovery Project bERLinPro, in: Proceedings of the sixth International Particle Accelerator Conference (IPAC'15), Richmond, USA, May 3-9, 2015, TUPWA018.
- [21] E. Jensen, C. Bracco, O. Brüning, R. Calaga, N. Catalan-Lasheras, B. Goddard, M. Klein, R. Torres-Sanchez, A. Valloni, Design Study of an ERL Test Facility in CERN, in: Proceedings of the fifth International Particle Accelerator Conference (IPAC'14), Dresden, Germany, Jun. 15-20, 2014, TUOBA02.
- [22] S. Sakanaka et al., Recent Progress in the Energy Recovery Linac Project in Japan, in: Proceedings of the first International Particle Accelerator Conference (IPAC'10), Kyoto, Japan, May 23-28, 2010, TUPE091.
- [23] R. Hajima, N. Nakamura, S. Sakanaka, Y. Kobayashi (Eds.), Design Study of the Compact ERL, KEK Report 2007-7/JAEA-Research 2008-032 (2008) [in Japanese]; <http://ccdb5fs.kek.jp/tiff/2007/0724/0724007.pdf>
- [24] S. Matuba, Y. Honda, X. Jin, T. Miyajima, M. Yamamoto, T. Uchiyama, M. Kuwahara, Y. Takeda, Japanese Journal of Applied Physics 51 (2012) 046402.
- [25] I.V. Bazarov and C. K. Sinclair, Phys. Rev. ST Accel. Beams 8 (2005) 034202.

- [26] General Particle Tracer, Pulsar Physics, <http://www.pulsar.nl/gpt/index.html>
- [27] I.V. Bazarov and T. Miyajima, Calculation of Coherent Synchrotron Radiation in General Particle Tracer, in: Proceedings of the eleventh European Particle Accelerator Conference (EPAC'08), Genoa, Italy, June 23-27, 2008, MOPC024.
- [28] T. Akagi, A. Kosuge, S. Araki, R. Hajima, Y. Honda, T. Miyajima, M. Mori, R. Nagai, N. Nakamura, M. Shimada, T. Shizuma, N. Terunuma, J. Urakawa, Phys. Rev. Accel. Beams 19 (2016) 114701.
- [29] M. Borland, "elegant: A Flexible SDDS-compliant Code for Accelerator Simulation", APS LS-287, Sep. 2000.
- [30] Ryoichi Hajima, Japanese Journal of Applied Physics 42 (2003) L974.
- [31] Y. Jiao, X. Cui, X. Huang, G. Xu, Phys. Rev. ST Accel. Beams 17 (2014) 060701.
- [32] M. Venturini, Phys. Rev. Accel. Beams 19 (2016) 064401.
- [33] B. Dunham, J. Barley, A. Bartnik, I. Bazarov, L. Cultera, J. Dobbins, G. Hoffstaetter, B. Johnson, R. Kaplan, S. Karkare, V. Kostroun, Y. Li, M. Liepe, X. Liu, F. Loehl, J. Maxson, P. Quigley, J. Reilly, D. Rice, D. Sabol, E. Smith, K. Smolenski, M. Tigner, V. Vesherevich, D. Widger and Z. Zhao, Appl. Phys. Lett. 102 (2013) 034105.
- [34] N. Nishimori, R. Nagai, S. Matsuba, R. Hajima, M. Yamamoto, Y. Honda, T. Miyajima, H. Iijima, M. Kuriki and M. Kuwahara, Appl. Phys. Lett. 102 (2013) 234103.
- [35] R. Nagai, R. Hajima, N. Nishimori, T. Muto, M. Yamamoto, Y. Honda, T. Miyajima, H. Iijima, M. Kuriki, M. Kuwahara, S. Okumi and T. Nakanishi, Rev. Sci. Instrum. 81 (2010) 033304.
- [36] N. Nishimori, R. Nagai, S. Matsuba, R. Hajima, M. Yamamoto, Y. Honda, T. Miyajima, H. Iijima, M. Kuriki and M. Kuwahara, Phys. Rev. ST Accel. Beams 17 (2014) 53401.
- [37] Y. Honda, Development of a Photo-injector Laser System for KEK ERL Test Accelerator, in: Proceedings of the third International Particle Accelerator Conference (IPAC'12), New Orleans, USA, May 20-25, 2012, TUPPD056.
- [38] S. Sakanaka et. al., Construction and Commissioning of Compact-ERL Injector at KEK, in: Proceedings of the 53th ICFA Advanced Beam Dynamics Workshop on Energy Recovery Linacs (ERL-2013), Novosibirsk, Russia, Sept. 9-13, 2013, WG102.
- [39] T. Takahashi et. al., Development of a 1.3-GHz Buncher Cavity for the Compact

ERL, in: Proceedings of the fifth International Particle Accelerator Conference (IPAC'14), Dresden, Germany, Jun. 15-20, 2014, THPRI045.

[40] S. Noguchi, E. Kako, M. Sato, T. Shishido, K. Watanabe and Y. Yamamoto, Present Status of Superconducting Cavity System in cERL Injector Linac at KEK, in: Proceedings of the first International Particle Accelerator Conference (IPAC'10), Kyoto, Japan, May 23-28, 2010, WEPEC024.

[41] K. Watanabe, E. Kako, S. Noguchi, T. Shishido, Nuclear Instruments and Methods in Physics Research A 734 (2014) 32.

[42] E. Kako, S. Noguchi, T. Shishido, K. Watanabe, Y. Yamamoto, High Power Tests of CW Input Couplers for cERL Injector Cryomodule, in: Proceedings of the third International Particle Accelerator Conference (IPAC'12), New Orleans, USA, May 20-25, 2012, WEPPC012.

[43] E. Kako, S. Noguchi, T. Shishido, K. Watanabe, Y. Yamamoto, Construction of Injector Cryomodule for cERL at KEK, in: Proceedings of the third International Particle Accelerator Conference (IPAC'12), New Orleans, USA, May 20-25, 2012, WEPPC015.

[44] K. Umemori, K. Enami, T. Furuya, H. Sakai, M. Satoh, K. Shinoe, M. Sawamura, E. Cenni, Construction of Main Linac Cryomodule for Compact ERL Project, in: Proceedings of the fourth International Particle Accelerator Conference (IPAC'13), Shanghai, China, May 12-17, 2013, WEPWO016.

[45] K. Umemori et al., Design of L-band Superconducting Cavity for the Energy Recovery Linacs, in: Proceedings of the fourth Asian Particle Accelerator Conference (APAC 2007), Indore, India, Jan. 29-Feb. 2, 2007, THC2MA03.

[46] H. Sakai, T. Furuya, N. Nakamura, K. Umemori, K. Shinoe, M. Sawamura, High Power Tests of KEK-ERL Input Coupler for Main Linac Under Liquid Nitrogen Condition, in: Proceedings of 15th International Conference on RF Superconductivity (SRF2011), Chicago, USA, Jul. 25-29, 2011, TUPO005.

[47] M. Sawamura, T. Furuya, H. Sakai, K. Umemori, K. Shinoe, E. Cenni, Cooling Properties of HOM Absorber Model for cERL in Japan, in: Proceedings of 15th International Conference on RF Superconductivity (SRF2011), Chicago, USA, Jul. 25-29, 2011, TUPO003.

[48] S. Noguchi, New Tuners for ILC Cavity Application, presentation slide in: Proceedings of 13th International Workshop on RF Superconductivity (SRF2007),

Beijing, China, Oct. 14-19, 2007, WE303.

[49] T. Miura, M. Akemoto, D. Arakawa, S. Fukuda, H. Honma, H. Katagiri, T. Matsumoto, H. Matsushita, S. Michizono, H. Nakajima, K. Nakao, F. Qiu, T. Shidara, T. Takenaka, Y. Yano, Performance of RF System for Compact ERL Injector in KEK, in: Proceedings of the 53th ICFA Advanced Beam Dynamics Workshop on Energy Recovery Linacs (ERL-2013), Novosibirsk, Russia, Sept. 9-13, 2013, WG306.

[50] T. Miura, M. Akemoto, A. Akiyama, D. Arakawa, S. Fukuda, H. Honma, H. Katagiri, T. Matsumoto, H. Matsushita, S. Michizono, H. Nakajima, K. Nakao, F. Qiu, H. Sakai, T. Shidara, T. Takenaka, K. Umemori, Y. Yano, Performance of RF System for Compact-ERL Main Linac at KEK, in: Proceedings of the fifth International Particle Accelerator Conference (IPAC'14), Dresden, Germany, Jun. 15-20, 2014, WEPME073.

[51] F. Qiu, D. Arakawa, H. Katagiri, T. Matsumoto, S. Michizono, T. Miura, Performance of the Digital LLRF System at the cERL, in: Proceedings of the fifth International Particle Accelerator Conference (IPAC'14), Dresden, Germany, Jun. 15-20, 2014, WEPME072.

[52] F. Qiu, S. Michizono, T. Miura, T. Matsumoto, M. Omet, B.W. Sigit, Phys. Rev. ST Accel. Beams 18 (2015) 092801.

[53] F. Qiu, D. Arakawa, Y. Honda, H. Katagiri, T. Matsumoto, S. Michizono, T. Miura, T. Obina, H. Sakai, S.B. Wibowo, Performance of the Digital LLRF Systems at KEK cERL, in: Proceedings of the 56th ICFA Advanced Beam Dynamics Workshop on Energy Recovery Linacs (ERL2015), Stony Brook, USA, June 7-12, 2015, WEIDLH2066.

[54] H. Nakai, K. Hara, T. Honma, K. Hosoyama, Y. Kojima, K. Nakanishi, T. Kanekiyo, S. Morita, Superfluid Helium Cryogenic Systems for Superconducting RF Cavities at KEK, in: AIP Conference Proceedings 1573 (2014) 1349.

[55] R. Takai, T. Obina, H. Sagehashi, Y. Tanimoto, T. Honda, T. Nogami, M. Tobiyama, Design and Initial Commissioning of Beam Diagnostic for the KEK compact ERL, in: Proceedings of the third International Beam Instrumentation Conference (IBIC 2014), Monterey, USA, Sep. 14-18, 2014, MOCYB2.

[56] Y. Honda, A. Aryshev, M. Shevelev, M. Shimada, R. Takai, T. Miyajima, Development of Bunch Length Monitor System at the Return Loop of KEK ERL Test Accelerator, in: Proceedings of the 11th Annual Meeting of Particle Accelerator Society of Japan, Aomori, Japan, Aug. 9-11, 2014, SAP089 [in Japanese].

- [57] A. Ueda, K. Harada, S. Nagahashi, T. Kume, M. Shimada, T. Miyajima, N. Nakamura, K. Endo, Design and Fabrication of the Compact ERL Magnets, in: Proceedings of the seventh International Particle Accelerator Conference (IPAC'16), Busan, Korea, May 8-13, 2016, TUPMB005.
- [58] N. Nakamura, M. Shimada, T. Miyajima, K. Harada, O.A. Tanaka, S. Sakanaka, Simulation Study on Bunch Compression and Decompression for the Compact ERL, in: Proceedings of the sixth International Particle Accelerator Conference (IPAC'15), Richmond, USA, May 3-9, 2015, TUPWA069.
- [59] K. Harada, T. Kume, S. Nagahashi, N. Nakamura, S. Sakanaka, A. Ueda, The Magnet and Power Supply System for the Compact-ERL, in: Proceedings of the sixth International Particle Accelerator Conference (IPAC'15), Richmond, USA, May 3-9, 2015, WEPMA055.
- [60] Y. Tanimoto, S. Asaoka, T. Honda, T. Nogami, T. Obina, R. Takai, Design of the cERL Vacuum System, in: Proceedings of the fourth International Particle Accelerator Conference (IPAC'13), Shanghai, China, May 12-17, 2013, THPFI012.
- [61] EPICS homepage, <http://www.aps.anl.gov/epics/>
- [62] M. Iwasaki, A. Akiyama, K. Furukawa, H. Kaji, T. Naito, T.T. Nakamura, J. Odagiri, S. Sasaki, Y. Iitsuka, N. Yoshifuji, K. Asano, M. Hirose, T. Aoyama, M. Fujita, T. Nakamura, K. Yoshii, The Construction Status of the SuperKEKB Control System, in: Proceedings of the 2015 International Conference on Accelerator & Large Experimental Physics Control Systems (ICALEPCS 2015), Melbourne, Australia, Oct. 17-23, 2015, MOB3O04.
- [63] T. Obina and C.O. Pak, Nuclear Instruments and Methods in Physics Research A 577 (2007) 417.
- [64] K. Yoshii, T. Nakamura, K. Furukawa, T.T. Nakamura, T. Obina, M. Satoh, N. Yamamoto, Web-Based Electronic Operation Log System – Zlog System, in: Proceedings of the 2007 International Conference on Accelerator & Large Experimental Physics Control Systems (ICALEPCS 2007), Knoxville, USA, Oct. 15-19, 2007, WOAB04.
- [65] S. Sakanaka, K. Haga, Y. Honda, H. Matsumura, T. Miyajima, T. Nogami, T. Obina, H. Sagehashi, M. Shimada, M. Yamamoto, Measurement and Control of Beam Losses Under High-Average-Current Operation of the compact ERL, in: Proceedings of the seventh International Particle Accelerator Conference (IPAC'16), Busan, Korea,

May 8-13, 2016, TUPOW038.

[66] N. Nakamura et al., Present Status of the Compact ERL at KEK, in: Proceedings of the fifth International Particle Accelerator Conference (IPAC'14), Dresden, Germany, Jun. 15-20, 2014, MOPRO110.

[67] N. Nishimori, R. Nagai, S. Matsuba, R. Hajima, M. Yamamoto, Y. Honda, T. Miyajima, H. Iijima, M. Kuriki, M. Kuwahara, Progress in a Photocathode DC Gun at the Compact ERL, in: Proceedings of the 35th International Free-Electron Laser Conference (FEL2013), New York, USA, Aug. 26-30, 2013, TUOCNO03.

[68] E. Kako, D. Arakawa, K. Hara, H. Katagiri, Y. Kojima, Y. Kondo, S. Michizono, T. Miura, H. Nakai, H. Nakajima, K. Nakanishi, S. Noguchi, T. Shishido, T. Takenaka, K. Watanabe, Y. Yamamoto, H. Hara, H. Hitomi, K. Sennyu, High Power Tests of Injector Cryomodule for Compact ERL, in: Proceedings of the fourth International Particle Accelerator Conference (IPAC'13), Shanghai, China, May 12-17, 2013, WEPWO013.

[69] K. Umemori, K. Enami, T. Furuya, H. Sakai, M. Satoh, K. Shinoe, M. Sawamura, E. Cenni, Construction of Main Linac Cryomodule for Compact ERL Project, in: Proceedings of the fourth International Particle Accelerator Conference (IPAC'13), Shanghai, China, May 12-17, 2013, WEPWO016.

[70] T. Honda, Y. Tanimoto, T. Nogami, R. Takai, T. Obina, S. Asaoka, T. Uchiyama, N. Nakamura, Vacuum system of the compact Energy Recovery Linac, AIP Conference Proceedings 1741 (2016) 020036.

[71] T. Miyajima, Y. Honda, M. Yamamoto, T. Uchiyama, K. Harada, M. Shimada, R. Takai, T. Kume, S. Nagahashi, T. Obina, A. Ueda, S. Sakanaka, N. Nakamura, N. Nishimori, R. Nagai, R. Hajima, J. Hwang, Low Emittance Electron Beam Transportation in Compact ERL Injector, in: Proceedings of the fifth International Particle Accelerator Conference (IPAC'14), Dresden, Germany, Jun. 15-20, 2014, THPRO093.

[72] J.-G. Hwang, E.-S. Kim, T. Miyajima, Y. Honda, K. Harada, M. Shimada, R. Takai, T. Kume, S. Nagahashi, T. Obina, N. Nakamura, S. Sakanaka, R. Hajima, R. Nagai, N. Nishimori, M. Yamamoto, T. Uchiyama, E. Kako, S. Michizono, T. Miura, Nuclear Instruments and Methods in Physics Research A753 (2014) 97.

[73] T. Miyajima, Y. Honda, R. Takai, T. Obina, M. Shimada, K. Harada, M. Yamamoto, K. Umemori, H. Sakai, T. Miura, F. Qiu, N. Nakamura, S. Sakanaka, N. Nishimori, R. Nagai, R. Hajima, D. Lee, Status of Higher Bunch Charge Operation in

Compact ERL, in: Proceedings of the sixth International Particle Accelerator Conference (IPAC'15), Richmond, USA, May 3-9, 2015, TUPWA067.

[74] M. Shimada, N. Nakamura, R. Takai, A. Ueda, T. Miyajima, Y. Honda, T. Obina, K. Harada, Optics Measurement of cERL Recirculation Loop, in: Proceedings of the 12th Annual Meeting of Particle Accelerator Society of Japan, August 5-7, 2015, Tsuruga, Japan, THP019 [in Japanese].

[75] M. G. Minty and F. Zimmermann, *Measurement and Control of Charged Particle Beams* (Springer, 2003), Chap. 4.

Figure caption

Fig. 1. Illustration of the compact ERL

Fig. 2. Schematic layout of the cERL injector.

Fig. 3. Normalized emittances and an rms bunch length at the exit from the merger after the optimization for the bunch charge of 80 pC.

Fig. 4. Optimized layout of the cERL injector. Under the staged optimization, the beamline is divided into three (injector, merger, and ML) sections.

Fig. 5. Optimization for the bunch charge of 7.7 pC. Normalized emittances at the exit from the injector section are shown as a function of the rms bunch length.

Fig. 6. Designed beam optics of the injector, optimized for the bunch charge of 7.7 pC. The upper plot shows the horizontal and the vertical normalized emittances (ε_{nx} , ε_{ny}) together with the rms bunch length (σ_z). The middle plot shows the horizontal and vertical betatron functions. The bottom plot shows the total beam energy.

Fig. 7. Configuration of the cERL beamline. The components in blue and red colors denote dipoles and quadrupoles, respectively.

Fig. 8. Schematic lattice of each arc section.

Fig. 9. Combination of the quadrupole strengths K of the triplet (Q1, Q2, Q3) as a function of the R_{11} element of a 6-dimensional transfer matrix through the arc. The other quadrupoles (Q4, Q5, Q6) are determined to be mirror-symmetric about the center of the arc. The K -value is defined by $B'L_Q/(B\rho)$, where L_Q is the quadrupole length, B' the field gradient, and $B\rho$ the rigidity of a particle.

Fig. 10. Simulation results for the horizontal normalized emittances at the exit from the first arc, as a function of the horizontal betatron function at the center of the arc. R_{11} was

set to 0.687. The CSR effect was included while the space-charge effect was not included. The computer code *elegant* was used with the number of macroparticles set to 10^5 .

Fig. 11. Designed optical functions in the arc section.

Fig. 12. Schematic of the path-length control using four steering kicks that yield a short-cut or a detour in the beam orbit.

Fig. 13. Betatron and dispersion functions along a beamline of the recirculation loop, that is, from point A (the exit from the ML) to the beam dump. The beam optics for the commissioning, without the beam focusing at the LCS section, is shown.

Fig. 14. Schematic view of the 500-kV photocathode DC gun.

Fig. 15. Schematic of the laser system. It consists of an oscillator, fiber-based amplifiers, and wavelength conversion. A fast gating system using Pockels cells (P.C.) is implemented for realizing the burst mode and the interlock system. Beam shaping and monitoring systems are implemented in the transport line.

Fig. 16. Side view of the low-energy beam transport.

Fig. 17. The cERL injector cryomodule.

Fig. 18. String assembly of three 2-cell cavities with six input couplers: (a) the assembled string in the class-10 clean room, and (b) the completed injector cryomodule that was installed in the beamline of the cERL injector.

Fig. 19. Schematic of the cERL ML cryomodule.

Fig. 20. ML cryomodule as installed in the cERL accelerator room.

Fig. 21. Configuration of rf sources of the injector.

Fig. 22. RF power sources in the ML. 16-kW-power (right) and 8-kW-power solid-state amplifiers are shown.

Fig. 23. Layout of the 2-K-temperature superfluid helium cryogenic system for the cERL. Helium compressors and a 10000-L-volume vessel with liquid nitrogen are not shown.

Fig. 24. Flow diagram of the 2-K-temperature superfluid helium cryogenic system for the cERL.

Fig. 25. Schematics of (a) the BPM duct and (b) the SCM duct. Gapless flanges, used in the other ducts, are used for these ducts. The rf shield of the SCM duct smoothly connects the duct with adjacent ones using a physical contact through high-precision fitting.

Fig. 26. (Upper) Illustration showing the BPM signal in the ML section under a burst beam. Signals of two burst beams, with the time difference of $\sim 0.3 \mu\text{s}$ (i.e., the recirculation time), are superimposed with the phase difference of π . (Lower) An example of output signals (in V) from the log-detection circuit as a function of time (in μs).

Fig. 27. Typical configuration of the cERL dipole chamber. Kapton film heaters are pasted on the chamber exterior surface for in-situ bakeout at 150°C .

Fig. 28. Configuration of the cERL control network.

Fig. 29. Illustration of the radiation shield for the cERL.

Fig. 30. Locations of radiation monitors and beam-loss monitors. Locations of beam collimators are also indicated by COL1 to COL5.

Fig. 31. Layout of the cERL at the end of March, 2016.

Fig. 32. Photograph of the cERL in the accelerator room.

Fig. 33. Beam optics of the injector (from the cathode to the exit from the ML), designed for the commissioning. Upper: normalized emittances and bunch length, middle: betatron functions, lower: total beam energy. Initial laser pulse length: 3 ps (rms; Gaussian), rf voltage of the buncher cavity: 30 kV. The space charge effect was neglected.

Fig. 34. Layout of the beam monitors and the other components as of March, 2016. Note that some of the beam monitors were absent at the time of initial commissioning in December, 2013.

Fig. 35. Fine tuning of the path length of the recirculation beam. Horizontal beam positions, measured with a screen monitor SCM-31 at the dump line, are shown by dots as a function of the path-length change in the recirculation loop. A solid line denotes the calculation result. The horizontal dispersion function was ~ 0.36 m (design) at the screen monitor.

Fig. 36. Difference between input (P_{in}) and reflected (P_{ref}) rf-powers of the main linac as a function of time under “beam loading” and “energy recovery” modes of operation. An offset was subtracted so that $\Delta(P_{in} - P_{ref}) = 0$ without beams. Traces a) and b) indicate the power difference in the upstream and downstream cavities, respectively. Trace c) indicate an average beam current.

Fig. 37. Measured dispersion functions, indicated by crosses, as compared to those of design.

Fig. 38. Measured fluctuation in the beam momentum during 50 minutes. Abscissa: time, ordinate: relative momentum deviation ($\Delta p/p$) in %.

Fig. 39. Locations where the emittance measurement was conducted. The symbols A to D indicate the measurement locations while the red and blue arrows indicate the

quadrupole magnet and the screen monitor used at each location, respectively.

Fig. 40. Result of the quadrupole-scan measurement at location C in Fig. 39. Each data point shows an average of 20 measurements with the corresponding standard deviation indicated by an error bar. Solid lines indicate fitted curves based on the weighted least squares method. The spatial resolution of the screen monitor was $62\ \mu\text{m}$, both for the horizontal and vertical beam sizes. The distance between the screen and the longitudinal center of the quadrupole magnet was $\sim 6\ \text{m}$.

Figures

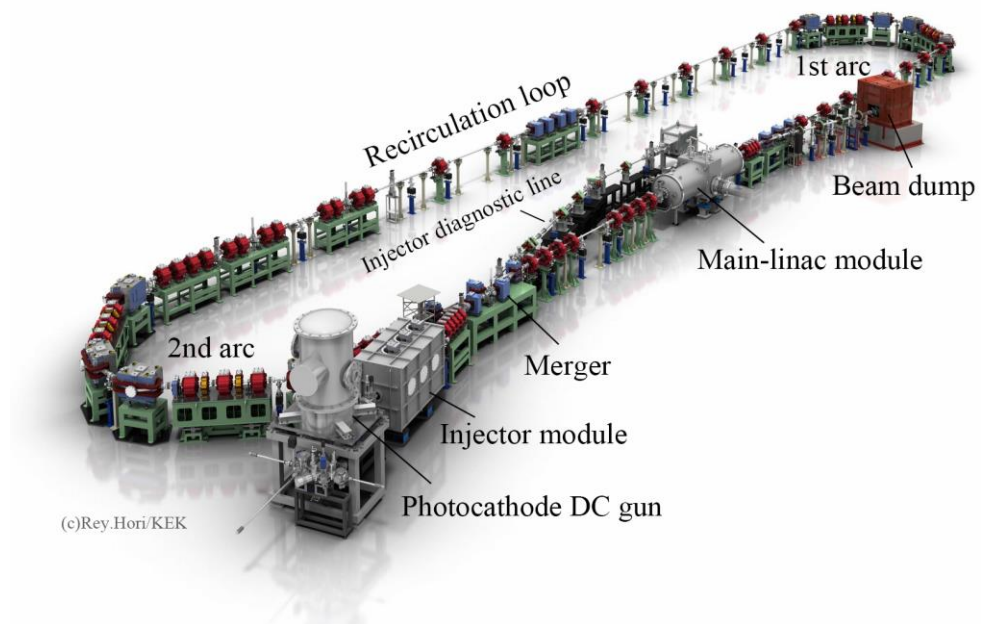


Fig. 1.

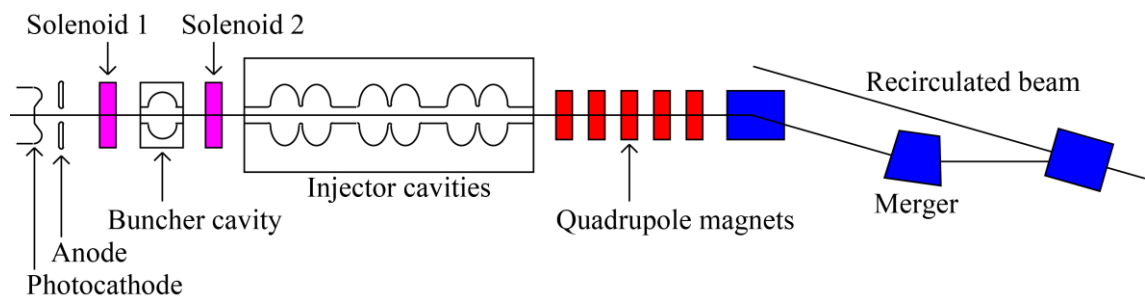


Fig. 2.

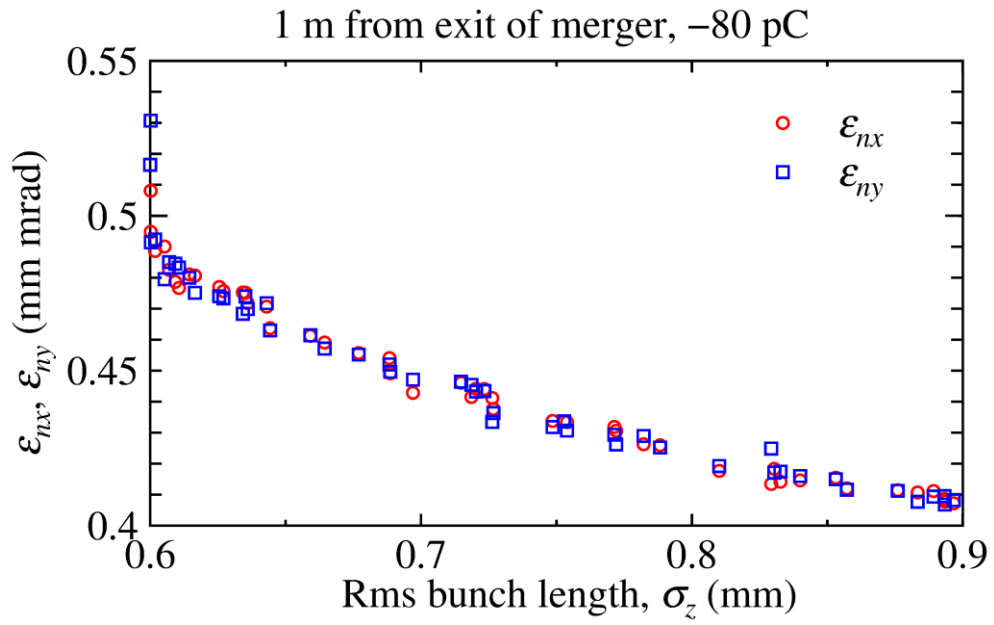


Fig. 3.

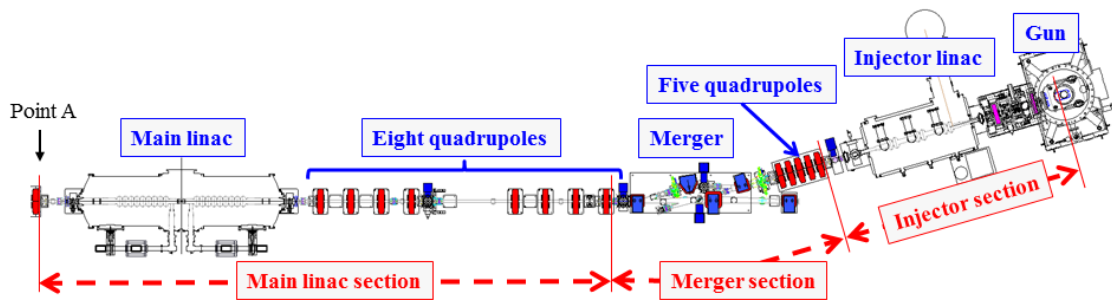


Fig. 4.

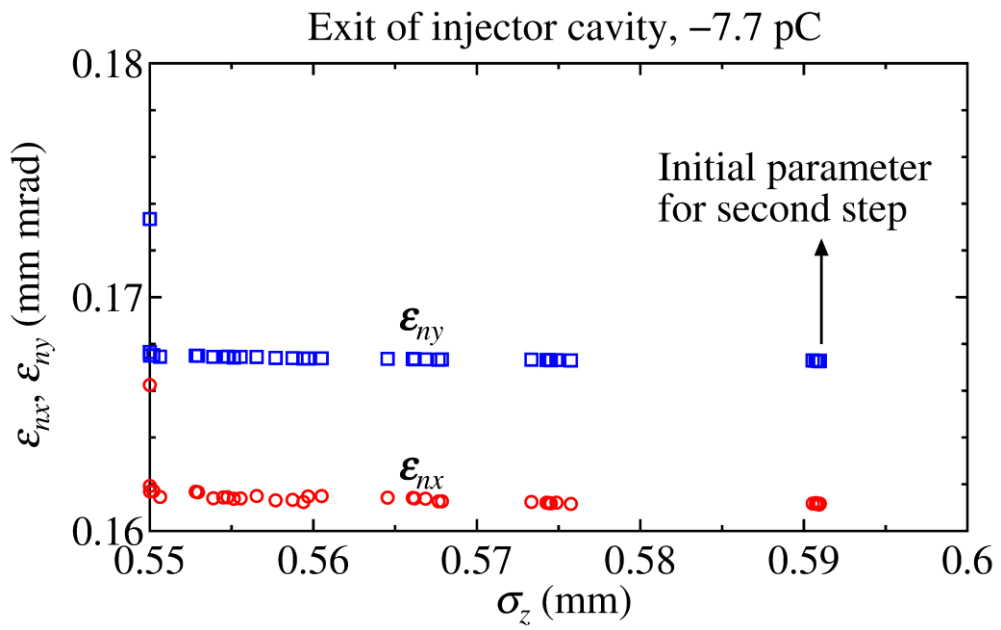


Fig. 5.

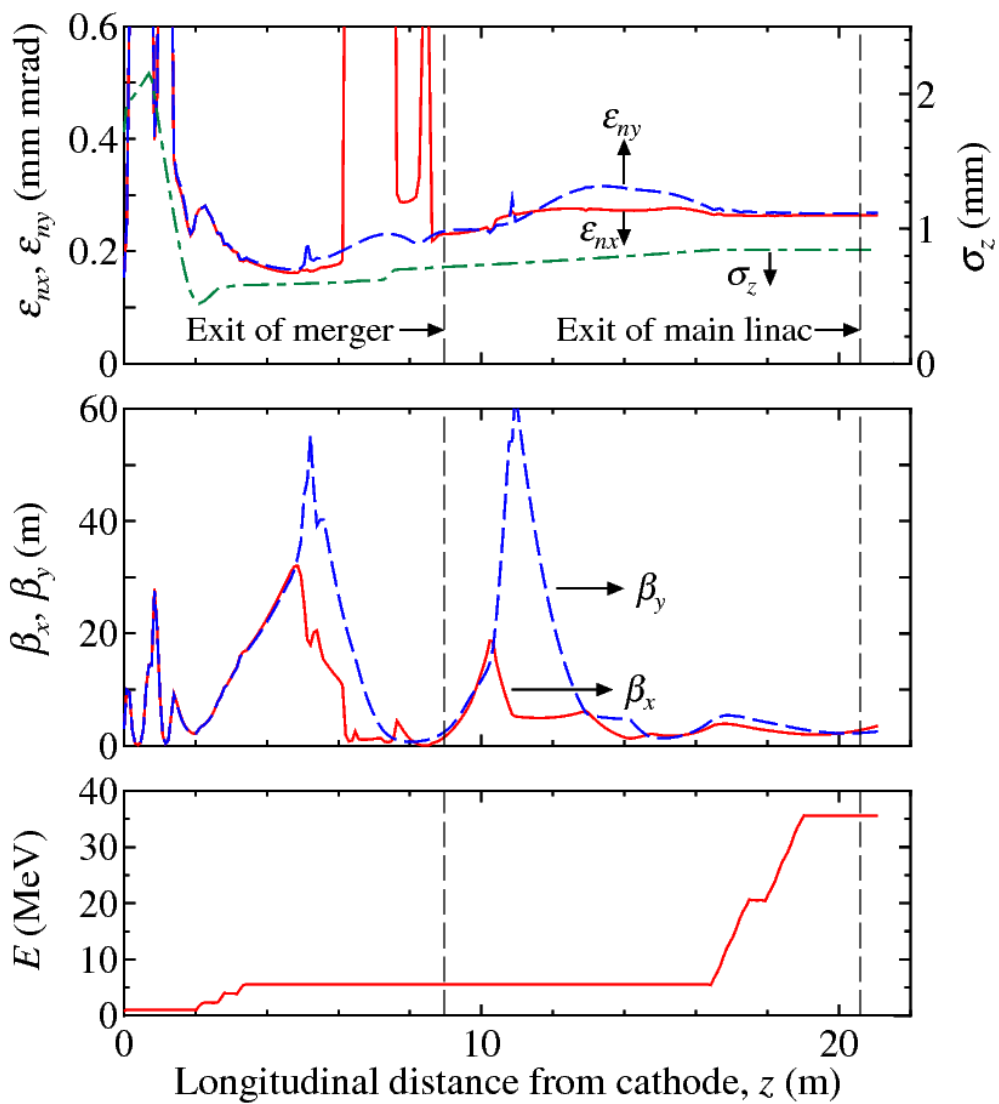


Fig. 6.

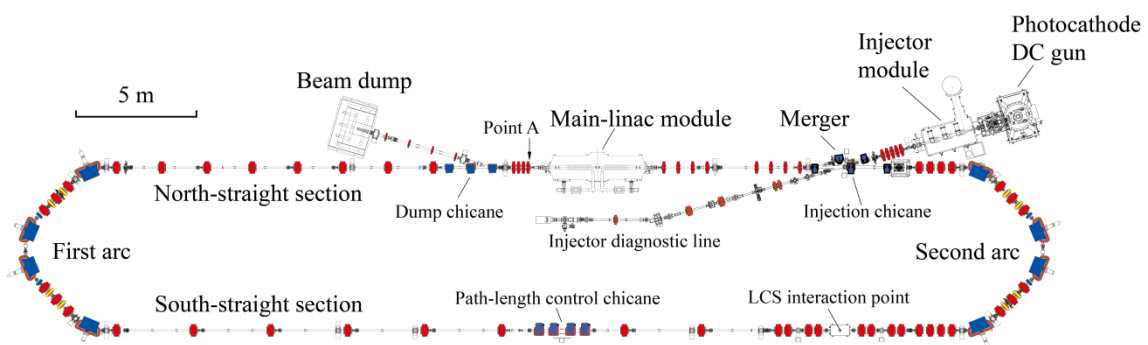


Fig. 7.

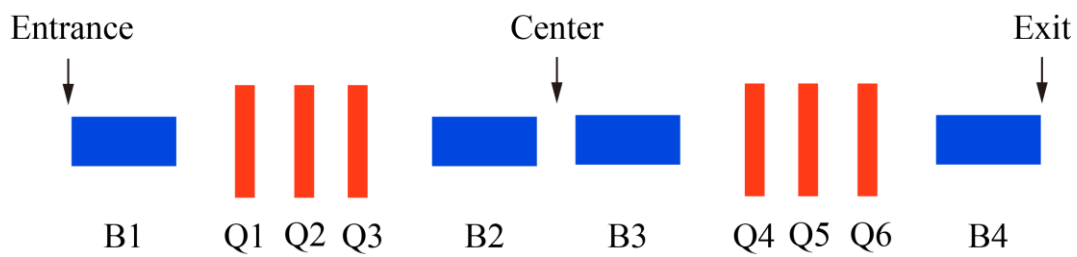


Fig. 8.

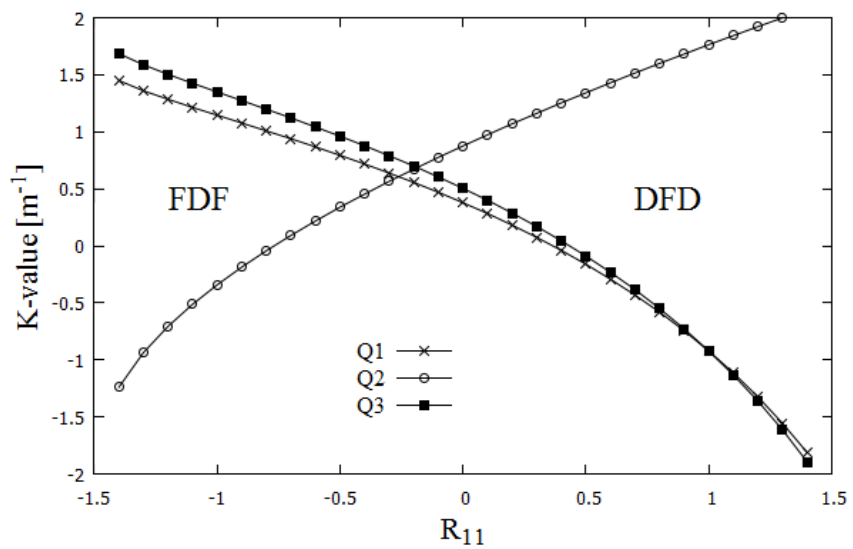


Fig. 9.

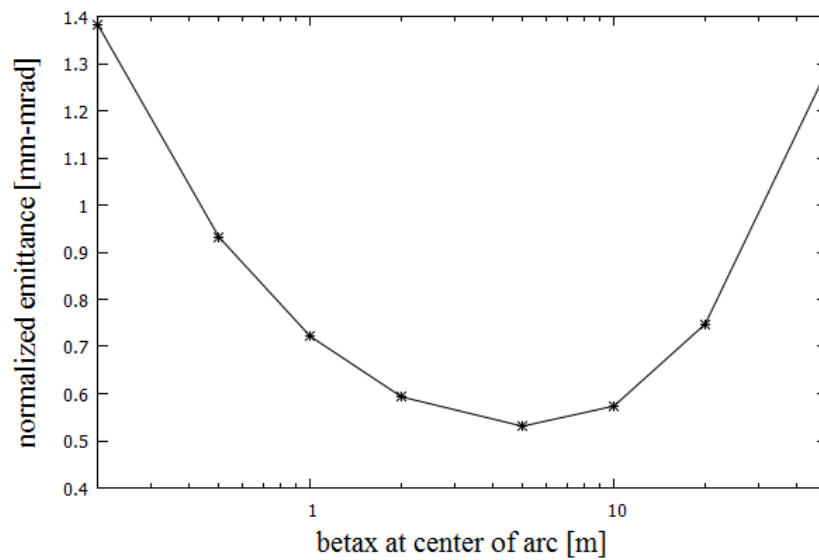


Fig. 10.

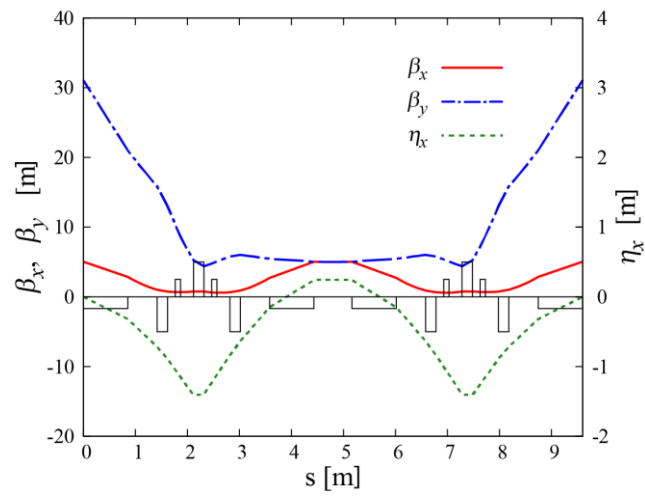


Fig. 11.

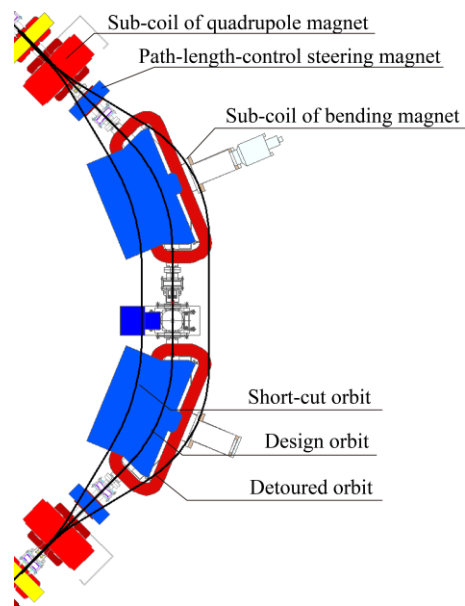


Fig. 12.

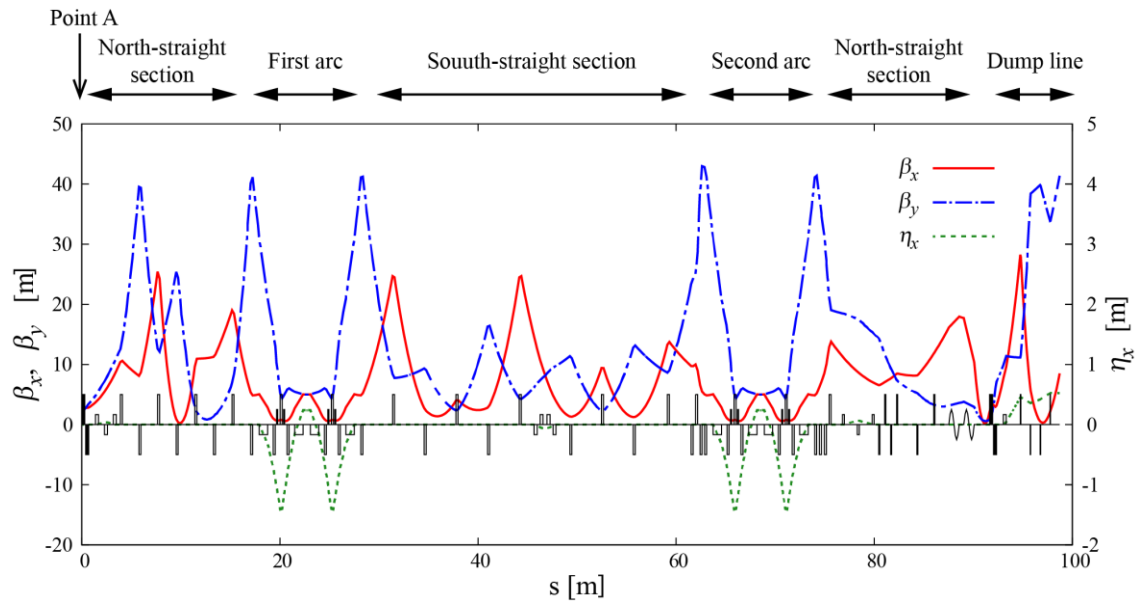


Fig. 13.

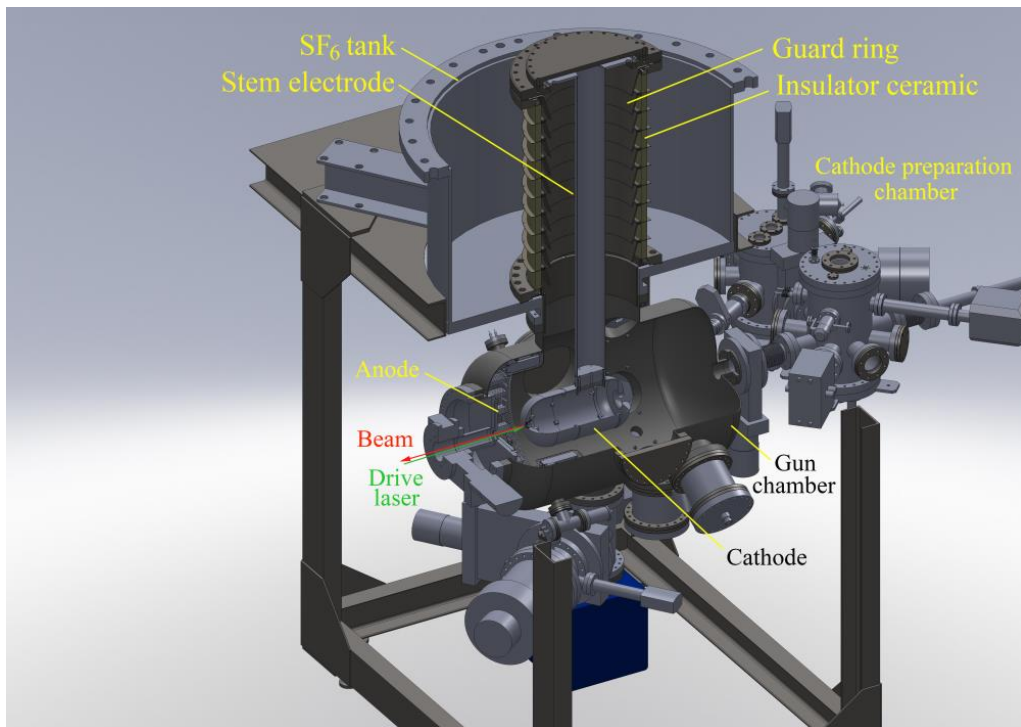


Fig. 14.

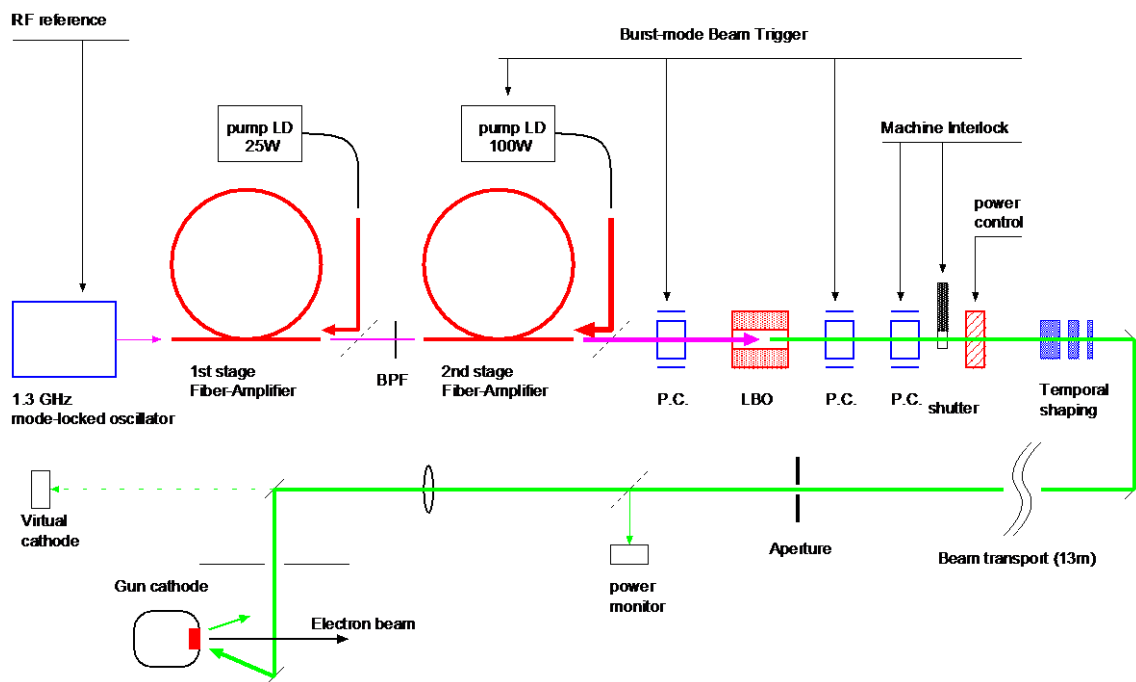


Fig. 15.

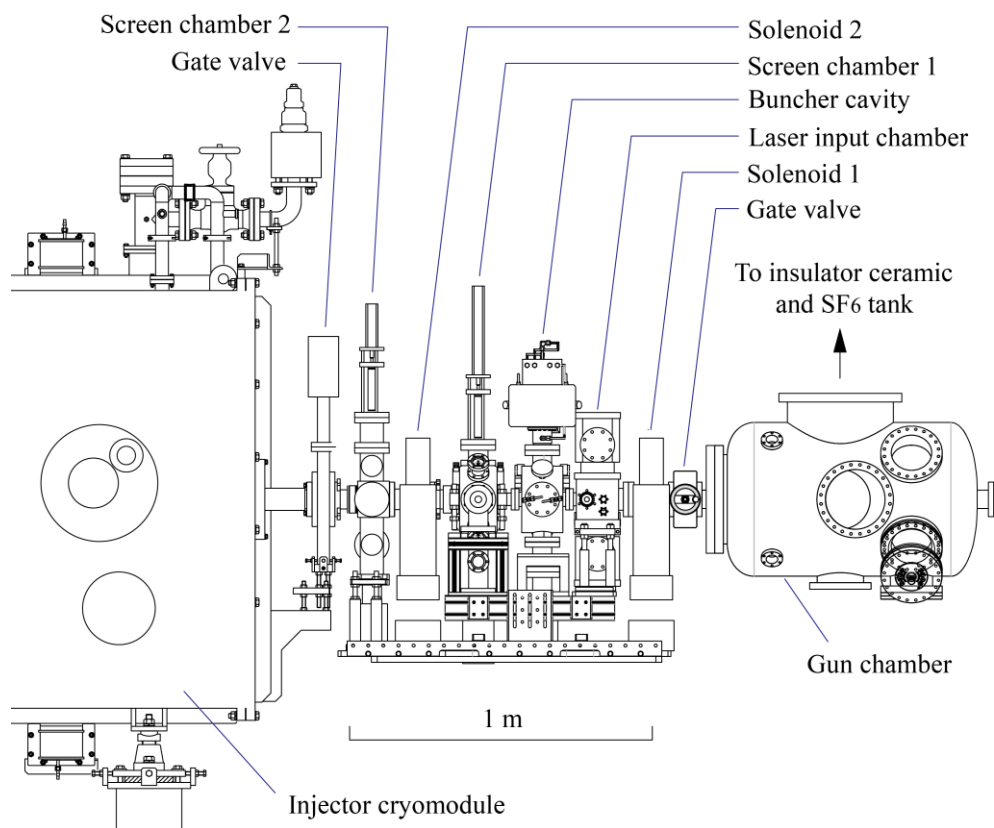


Fig. 16.

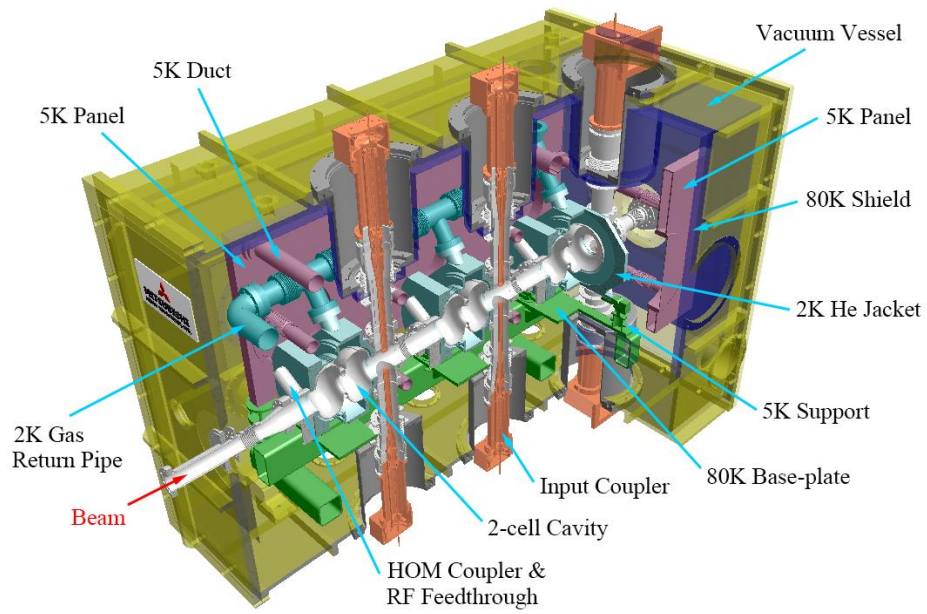


Fig. 17.



Fig. 18.

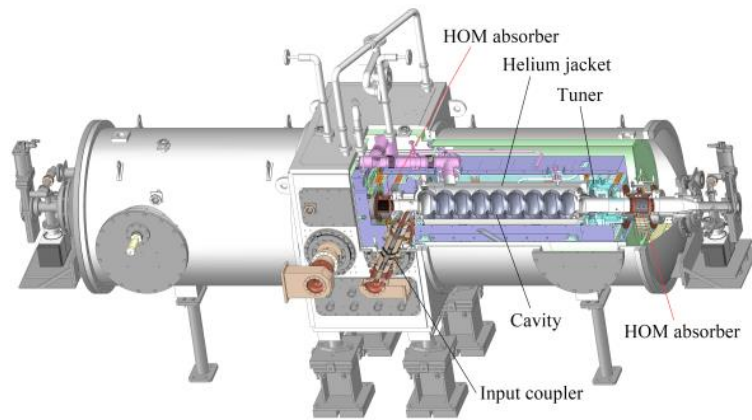


Fig. 19.



Fig. 20.

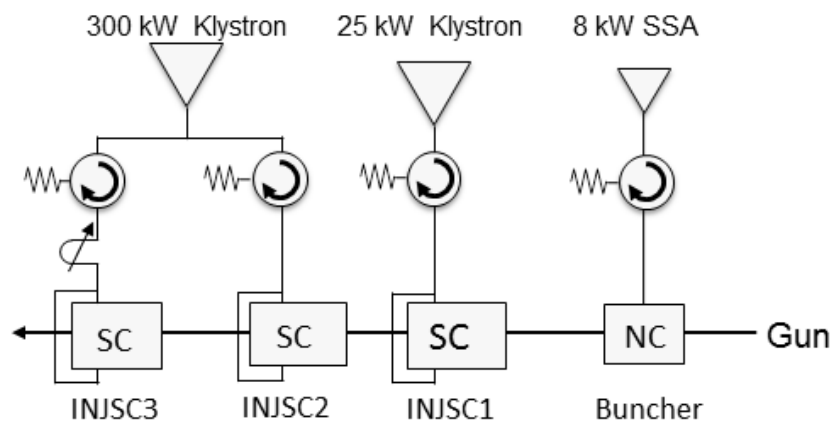


Fig. 21.



Fig. 22.

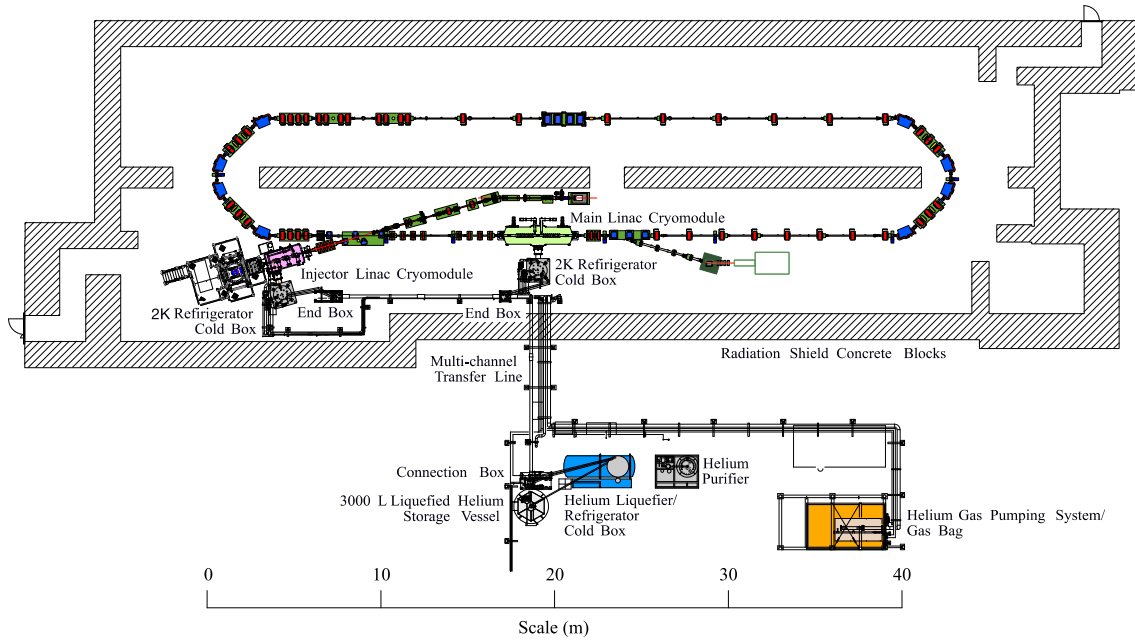


Fig. 23.

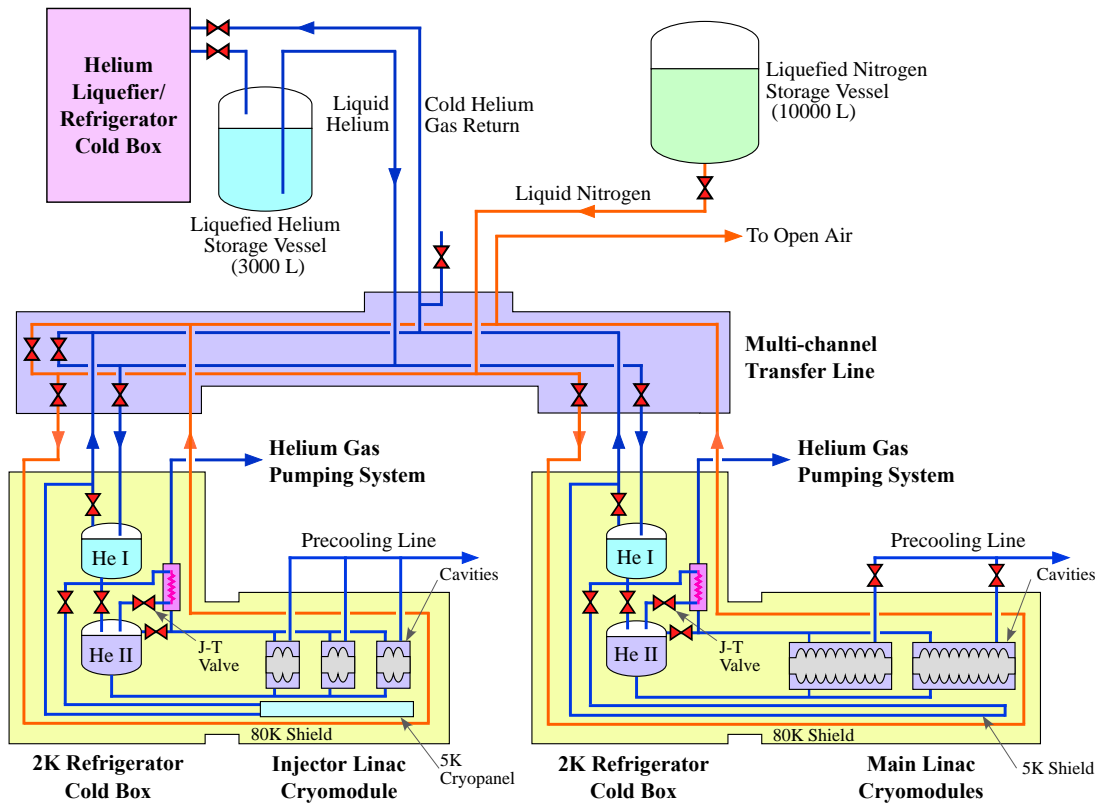


Fig. 24.

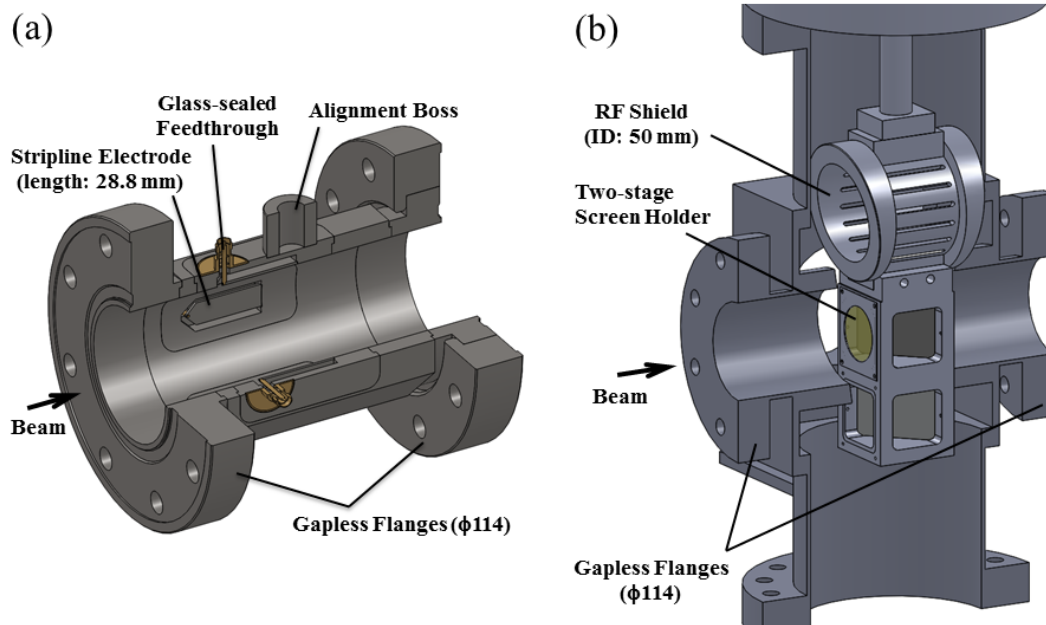


Fig. 25.

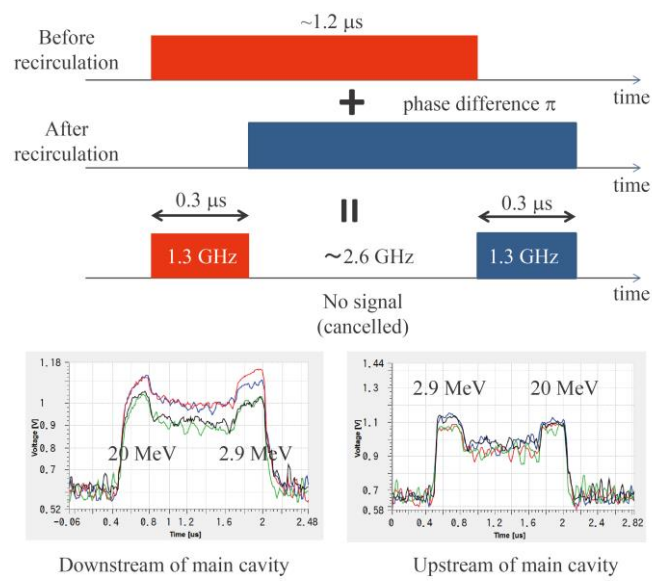


Fig. 26.

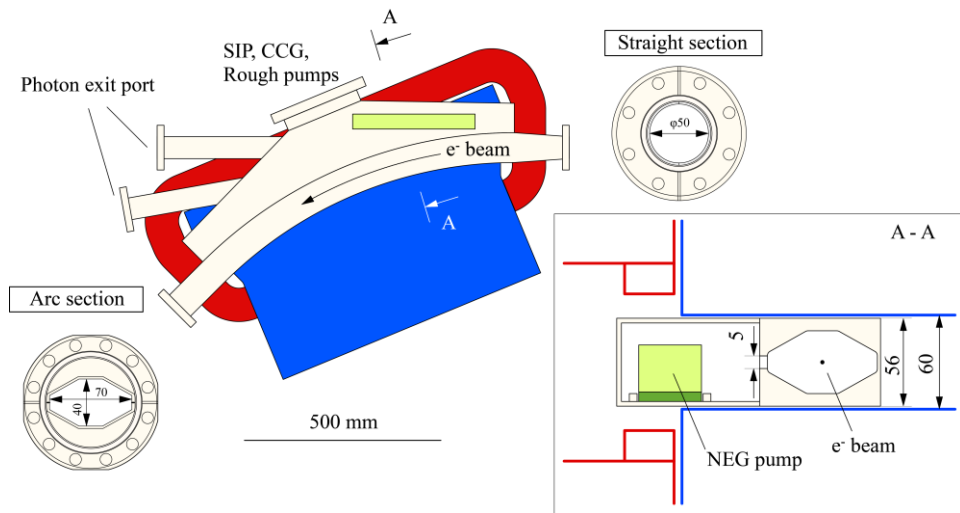


Fig. 27.

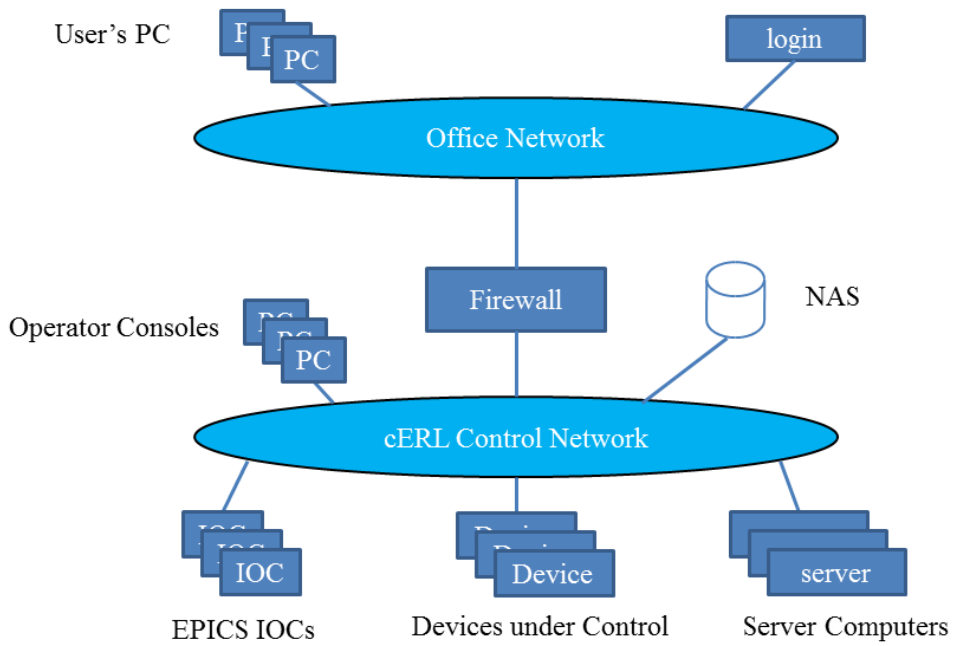


Fig. 28.

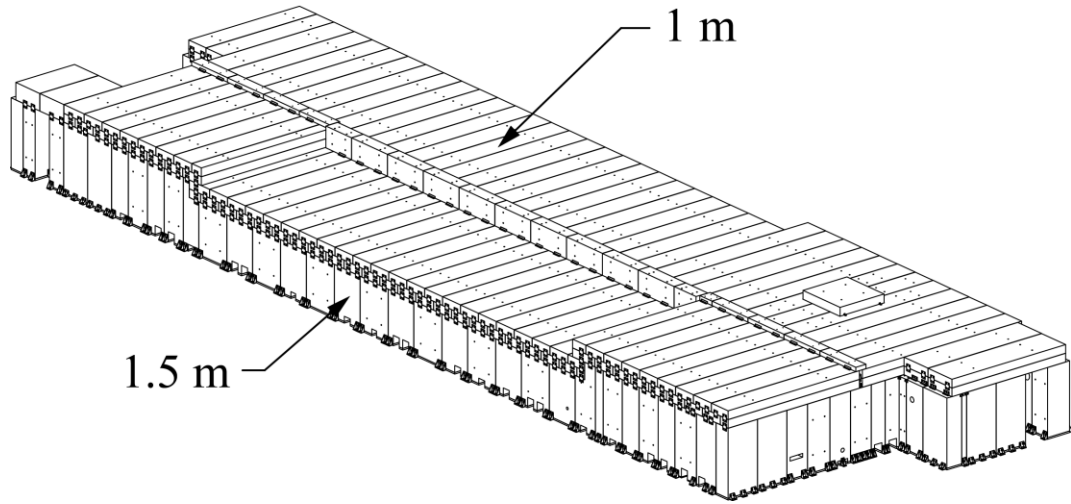


Fig. 29.

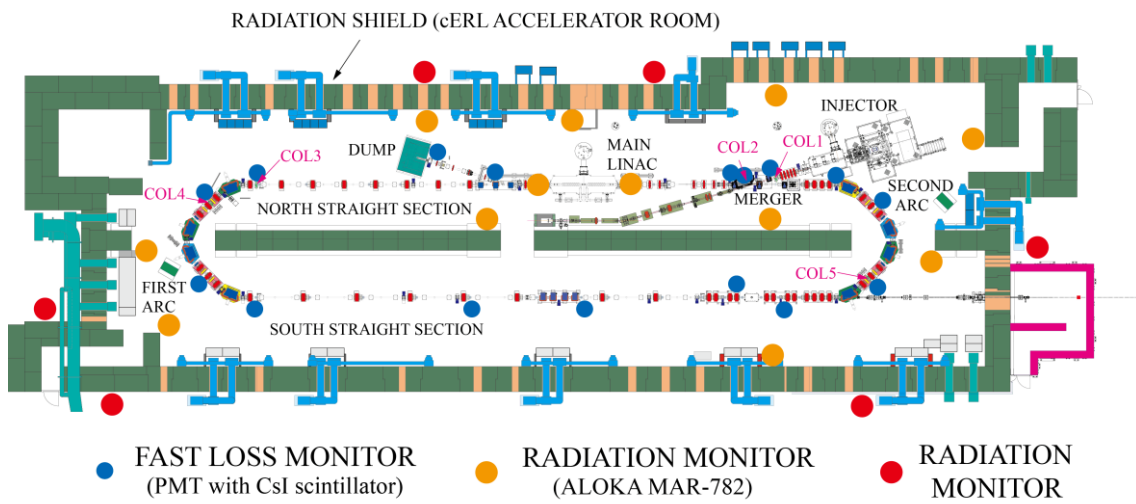


Fig. 30.

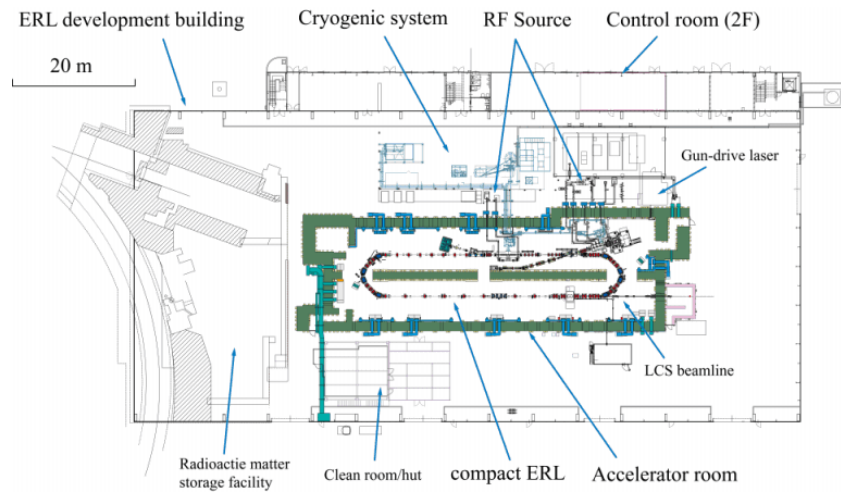


Fig. 31.

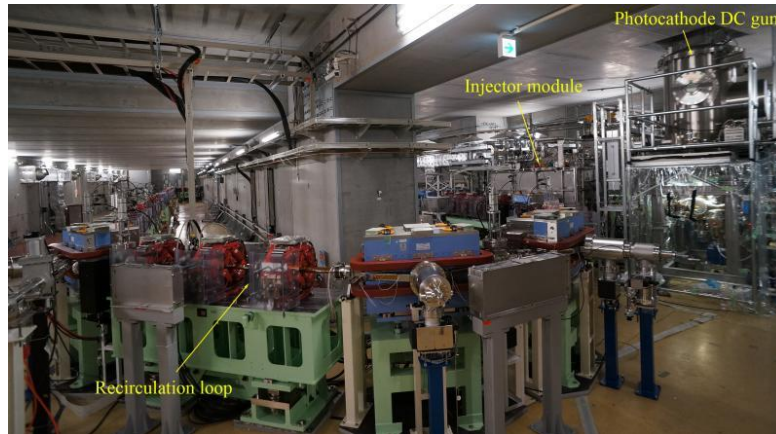


Fig. 32.

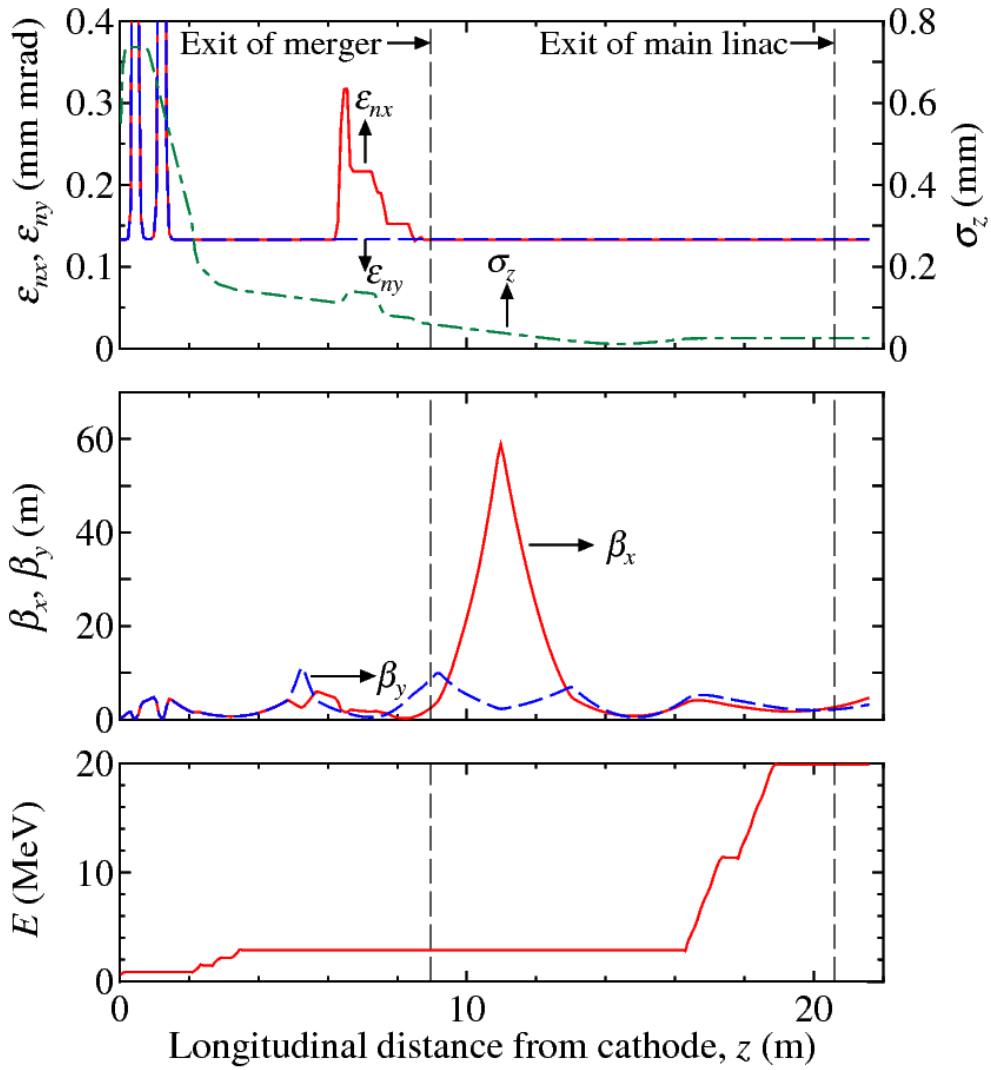


Fig. 33.

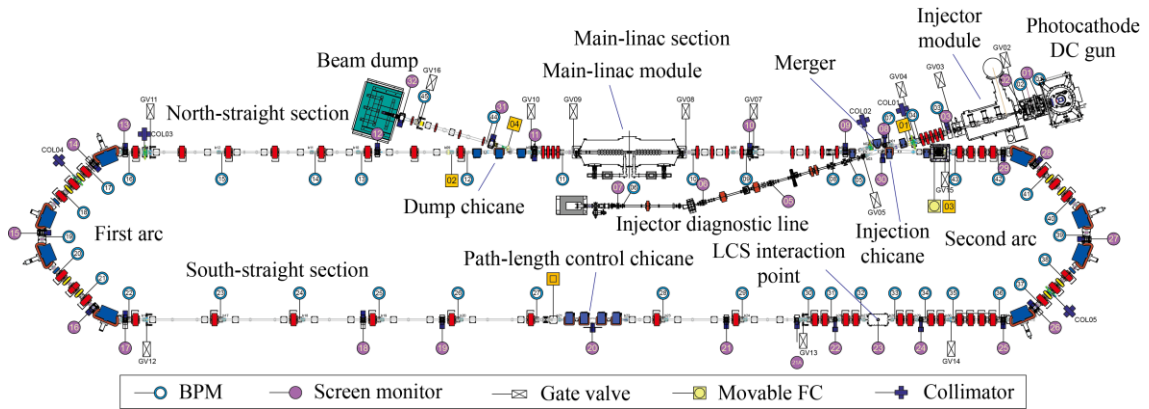


Fig. 34.

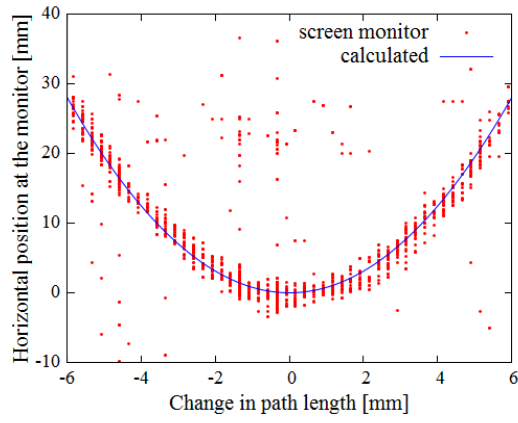


Fig. 35.

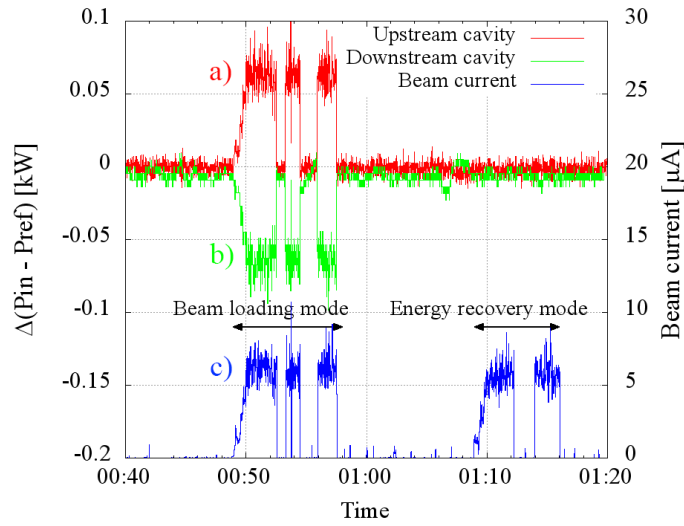


Fig. 36.

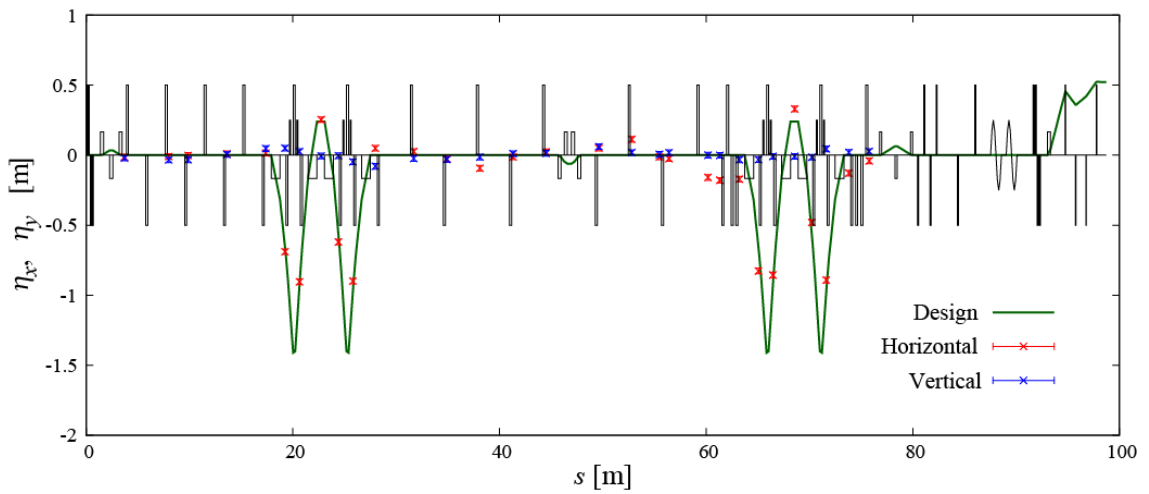


Fig. 37.

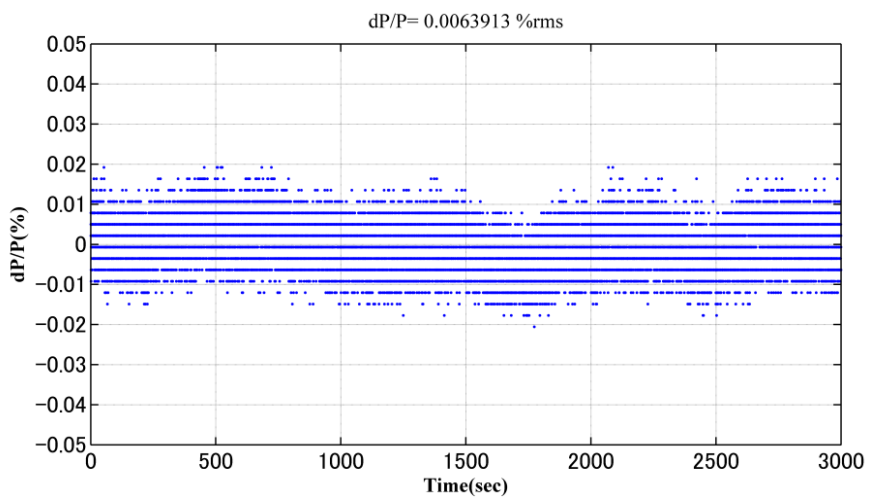


Fig. 38.

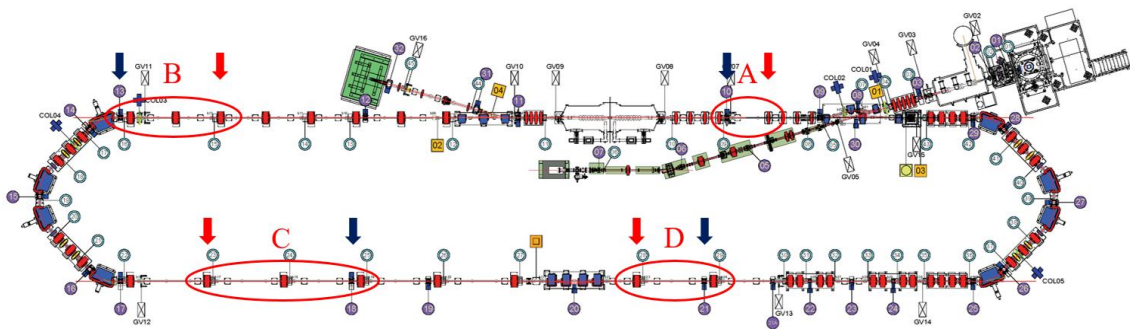


Fig. 39.

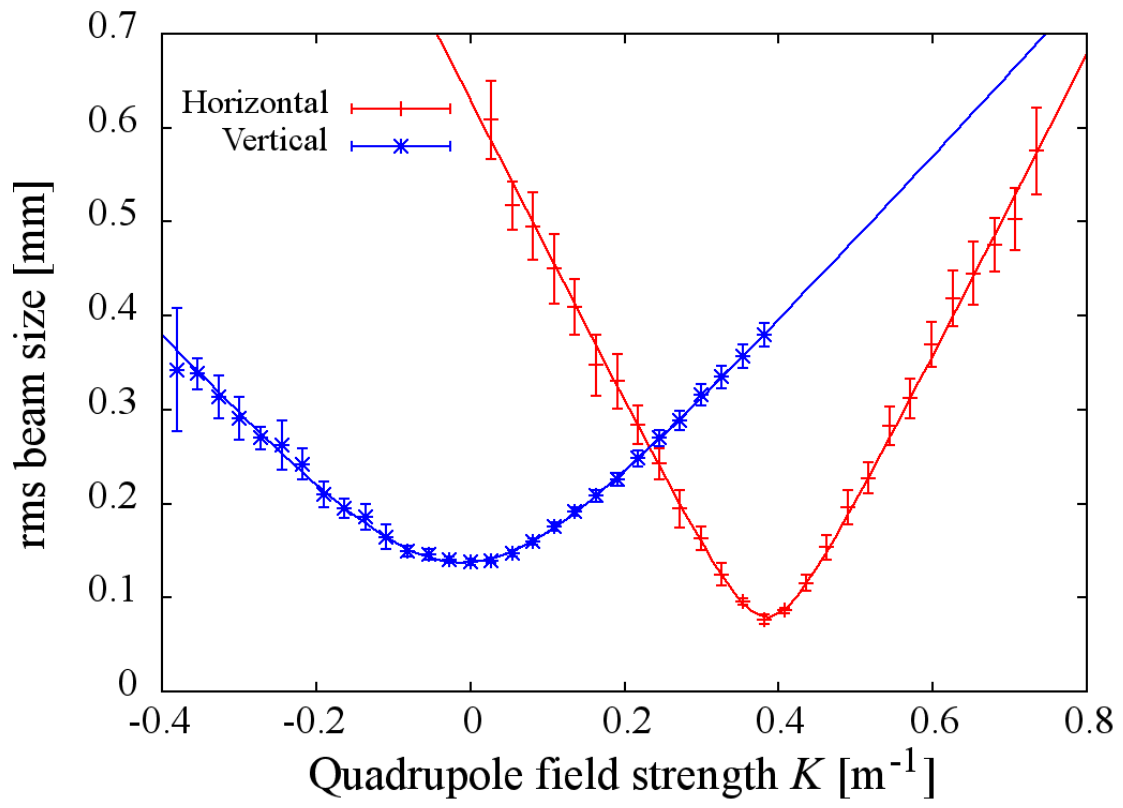


Fig. 40.

Tables

Table 1 Design parameters of the compact ERL.

Beam energy ^a E	35 MeV
Average beam current I_0	10 mA
Injection energy ^a E_{inj}	5.5 MeV
Accelerating gradient in ML cavities E_{acc}	15 MV/m
Rms normalized emittance (@charge/bunch) ϵ_n	0.3 mm·mrad (@7.7 pC) 1 mm·mrad (@77 pC)
Rms bunch length σ_τ	1 – 3 ps 100 fs (with bunch compression)
RF frequency f_{rf}	1.3 GHz
Repetition frequency of bunches f_b	1.3 GHz (for usual operation) 162.5 MHz (for LCS experiment)

^a Total energy is used in this paper

Table 2 Optimized element positions of the cERL injector (from the gun to the entrance to the merger).

Element	Distance^a from cathode (m)
Solenoid 1	0.445
Buncher cavity	0.809
Solenoid 2	1.217
Injector cavity 1	2.221
Injector cavity 2	2.781
Injector cavity 3	3.341
Quadrupole 1	4.854
Quadrupole 2	5.054
Quadrupole 3	5.254
Quadrupole 4	5.454
Quadrupole 5	5.654

^a Distance from the cathode to the center of each element

Table 3 Beamline parameters of the cERL injector, optimized for the bunch charge of 7.7 pC.

Parameter	Value
Gun voltage	500 kV
Initial laser-spot diameter ^a D	0.525 mm
Initial laser pulse length (FWHM)	16 ps
Magnetic field of solenoid 1	0.036 T
Magnetic field of solenoid 2	0.015 T
RF voltage of buncher cavity	105 kV
Phase ^b of buncher cavity	-90.0 degree
Accelerating gradient (E_{acc}) of injector cavity 1	6.8 MV/m
Phase ^b of injector cavity 1	29.9 degree
E_{acc} of injector cavity 2	7.53 MV/m
Phase ^b of injector cavity 2	-9.8 degree
E_{acc} of injector cavity 3	7.07 MV/m
Phase ^b of injector cavity 3	-10.0 degree

^a Rms spot size is given by $\sigma_{x,L} = D/4$ in the case of uniform distribution.

^b An electron bunch is at the crest when the phase is zero; the tail of the bunch is less accelerated when the phase is slightly positive.

Table 4 Specifications of the cryogenic system in JFY2014.

Parameter	Value
Refrigeration capacity at 4.4 K (nominal)	500 W
Liquefaction rate at 4.4 K (nominal)	250 L/h
Refrigeration capacity at 2.0 K (effective)	80 W
Helium compressor capacity (nominal)	86292 Nm ³ /day

Table 5 List of cERL beam monitors.

Monitor type	Objective	Number
Beam position monitor (stripline/button)	Position, charge	45
Screen monitor (Ce:YAG/OTR)	Position, charge	32
Beam loss monitor (fiber and PMT)	Loss	2
(scintillator and PMT)	Loss	27
Current transformer ^a	Charge	4
DC current transformer ^a	Current	1
Movable Faraday cup ^b	Charge	3

^a Both CTs and DCCT are currently not used because of the low beam current.

^b In addition to these FCs, both injector and main beam dumps are used as a Faraday cup.

Table 6 Progress of the cERL construction.

Period	Event
March, 2009 to March, 2010	Refurbishment of building
July, 2010 to March, 2011	Removal of radioactive matter from the building
March to September, 2012	Construction of the cERL accelerator room
June, 2012	Installation of the injector cryomodule
October, 2012	Installation of the ML cryomodule
October, 2012 to March, 2013	Installation and test of the photocathode DC gun
	Installation of the beamline components of the injector
April to June, 2013	Commissioning of the injector
July to November, 2013	Construction of the recirculation loop
December, 2013	Commissioning of the cERL, including the recirculation loop

Table 7 Parameters used for the initial commissioning of the cERL.

Beam energy E	19.9 MeV
Injection energy E_{inj}	2.9 MeV
Accelerating gradient (E_{acc}) in the injector cavities	2.9 – 3.3 MV/m
E_{acc} in the ML cavities	8.2 MV/m
Cathode voltage of the DC gun	390 kV
Laser pulse length	3 ps (rms)
Rf voltage in the buncher cavity	0 or 30 kV
Repetition frequency of bunches	1.3 GHz
Charge per bunch	< 100 fC
Normalized emittance at the cathode (estimated)	0.13 mm·mrad

Table 8 Measurement results of the normalized beam emittance (units: mm·mrad), at a low bunch charge of ~14 fC. Measurement errors were deduced from fitting errors. The beam energy at each location is also shown for reference.

Measurement location	Horizontal	Vertical	Beam energy (MeV)
A	0.147±0.010	0.138±0.004	2.9
B	0.144±0.004	0.123±0.003	19.9
C	0.139±0.005	0.135±0.003	19.9
D	0.132±0.004	0.153±0.003	19.9